

Ultrafast decoupling of polarization and strain in ferroelectric BaTiO₃

Le Phuong Hoang^{1,2,3}, David Pesquera⁴, Gerard N. Hinsley⁵, Robert Carley¹, Laurent Mercadier¹, Martin Teichmann¹, Saptam Ganguly⁴, Teguh Citra Asmara¹, Giacomo Merzoni^{6,1}, Sergii Parchenko¹, Justine Schlappa¹, Zhong Yin¹, José Manuel Caicedo Roque⁴, José Santiso⁴, Irena Spasojevic⁷, Camille Carinan¹, Tien-Lin Lee⁸, Kai Rosnagel^{3,9}, Jörg Zegenhagen⁸, Gustau Catalan^{4,10}, Ivan A. Vartanyants⁵, Andreas Scherz¹, and Giuseppe Mercurio^{1,*}

*giuseppe.mercurio@xfel.eu

¹European XFEL, 22869 Schenefeld, Germany

²Max Planck Institute for the Structure and Dynamics of Matter, 22761 Hamburg, Germany

³Institute of Experimental and Applied Physics, Kiel University, 24098 Kiel, Germany

⁴Catalan Institute of Nanoscience and Nanotechnology (ICN2), CSIC and BIST, Campus UAB, Bellaterra, 08193 Barcelona, Spain

⁵Deutsches Elektronen-Synchrotron DESY, 22607 Hamburg, Germany

⁶Dipartimento di Fisica, Politecnico di Milano, 20133, Milano, Italy

⁷Department de Física, Universitat Autònoma de Barcelona, 08193 Bellaterra, Spain

⁸Diamond Light Source Ltd., Didcot, OX110DE Oxfordshire, United Kingdom

⁹Ruprecht Haensel Laboratory, Deutsches Elektronen-Synchrotron DESY, 22607 Hamburg, Germany

¹⁰Institucio Catalana de Recerca i Estudis Avançats (ICREA), 08010 Barcelona, Catalonia

ABSTRACT

1 A fundamental understanding of the interplay between lattice structure, polarization and electrons is pivotal to the optical
2 control of ferroelectrics. The interaction between light and matter enables the remote and wireless control of the ferroelectric
3 polarization on the picosecond timescale, while inducing strain, i.e., lattice deformation. At equilibrium, the ferroelectric
4 polarization is proportional to the strain, and is typically assumed to be so also out of equilibrium. Decoupling the polarization
5 from the strain would remove the constraint of sample design and provide an effective knob to manipulate the polarization
6 by light. Here, upon an above-bandgap laser excitation of the prototypical ferroelectric BaTiO₃, we induce and measure an
7 ultrafast decoupling between polarization and strain that begins within 350 fs, by softening Ti-O bonds via charge transfer, and
8 lasts for several tens of picoseconds. We show that the ferroelectric polarization out of equilibrium is mainly determined by
9 photoexcited electrons, instead of the strain. This excited state could serve as a starting point to achieve stable and reversible
10 polarization switching via THz light. Our results demonstrate a light-induced transient and reversible control of the ferroelectric
11 polarization and offer a pathway to control by light both electric and magnetic degrees of freedom in multiferroics.

Ferroelectric materials are characterized by many properties, including piezoelectricity and pyroelectricity, besides ferroelectricity, which make them attractive for a wide range of applications, such as nonvolatile memories, transistors, sensors, and actuators^{1,2}. The key property of a ferroelectric material is the ability to switch its spontaneous polarization in response to an external electric field. This is typically achieved by a static or pulsed electric field with the consequent limitations given by the need for complex circuitry and switching times of hundreds of picoseconds to nanoseconds³. These challenges can be overcome by optical control of the ferroelectric polarization. Light-matter interaction enables remote and wireless control of the ferroelectric polarization on the picosecond timescale³. Moreover, since all ferroelectrics are also piezoelectrics, the ferroelectric polarization is strongly coupled to the strain, i.e., the lattice deformation⁴. Optical control of polarization and strain has been achieved in several cases. For example, in multilayers of ferroelectric and electrode thin films, an optical laser was used to excite the metal (or semiconductor) layer and indirectly the ferroelectric material, leading to a transient modification of the strain⁵⁻⁸, or the polarization by charge redistribution at the interface⁹. In other studies, light was absorbed directly by the ferroelectric material, inducing changes in the spontaneous polarization^{10,11} or lattice strain in clamped¹²⁻¹⁸ or freestanding¹⁹ ferroelectric thin films. THz light was employed to rotate²⁰ or even transiently reverse the orientation of the spontaneous polarization²¹. In all these studies so far, either the polarization or the strain was measured, and a direct proportionality between spontaneous polarization and strain was typically assumed²². This proportionality is based on the piezoelectric effect, which is well captured by the Landau-Ginzburg-Devonshire theory when the lattice distortion is along the polarization axis²³. While this assumption is valid under equilibrium conditions, as demonstrated experimentally, e.g. in Refs.^{24,25}, it may not hold under out-of-equilibrium conditions following light-matter interaction. Decoupling the polarization from the strain would remove the constraint of sample design to achieve specific properties^{24,26}, and, at the same time, would provide a more effective and ultrafast knob to manipulate the polarization by light.

To explore this scenario, we probe the out-of-plane strain and the spontaneous polarization of the prototypical ferroelectric BaTiO₃ upon above-bandgap absorption of ultrashort UV light pulses (Figure 1a). A fundamental understanding of the relationship between strain and ferroelectric polarization out of equilibrium requires their investigation on their natural timescale encompassing ≈ 100 fs to several tens of ps. We employ a combination of time-resolved X-ray diffraction (tr-XRD), time-resolved optical second harmonic generation (tr-SHG), and time-resolved optical reflectivity (tr-refl) to obtain the magnitudes and the separate dynamics of the out-of-plane lattice parameter, the spontaneous polarization, and the photoexcited carrier density, respectively²⁷, with a time resolution of ≈ 90 fs. In this paper, we will show the mechanisms that govern the structure and polarization changes in a ferroelectric material and their complex relationship out of equilibrium in the presence of photoexcited electrons and lattice deformation. In particular, since the strain wave propagates at the speed of sound, whereas electronic interactions are much faster, we induce and measure an ultrafast decoupling between polarization and strain, which we assign to the photoexcited electrons. First, we present the lattice response to the absorption of UV laser pulses and the corresponding data modeling. Next, we present tr-SHG and tr-refl data. Finally, we bring together all the results and discuss the underlying physical mechanisms in the context of hitherto known phenomena taking place in ferroelectric materials.

Results

Photoinduced structural dynamics

Our sample consists of a coherently strained, monodomain BaTiO₃ (BTO) thin film, grown on a GdScO₃ (GSO) substrate, with a SrRuO₃ (SRO) bottom electrode sandwiched in between (see Methods). Under a compressive strain of -0.55% imposed by the substrate, the BTO film shows an out-of-plane ferroelectric polarization P_s pointing toward the sample surface (Figure 1a). The sample is excited above the BTO band gap $E_g = 3.4\text{ eV}$ ²⁸ using 266 nm laser pulses at an incident pump laser fluence of 2.7 mJcm^{-2} . Time-resolved X-ray diffraction of the (001) Bragg reflection is employed to probe the lattice response of our ferroelectric thin film along the out-of-plane direction. The lattice deformations along the in-plane directions on the picosecond timescale are negligible, given the large ratio between photoexcited area ($330 \times 240\ \mu\text{m}^2$) and BTO film thickness $d_{\text{BTO}} = 34.5\text{ nm}$.

We observe an initial reduction of the tetragonal distortion, which goes hand in hand with lattice compression, then followed by lattice expansion. In particular, Figure 1b shows the (001) diffraction intensity I_{XRD} of BTO as a function of the photon energy E_V and at different pump-probe delays t from -14 ps to 32.5 ps . At $t = 2.6\text{ ps}$ we observe the following changes to the Bragg peak as compared to the ground state (at $t = -14\text{ ps}$): a decrease in the diffraction intensity I_{XRD} near the peak center, and a shift to higher photon energy, which implies a decrease in the out-of-plane lattice parameter c , i.e., lattice compression (see gray curve in Figure 1b). To further explore this initial structural dynamics, we measure the delay dependence of $\Delta I_{\text{XRD}}/I_{\text{XRD},0} = [I_{\text{XRD}}(t) - I_{\text{XRD},0}]/I_{\text{XRD},0}$, which quantifies the relative change of $I_{\text{XRD}}(t)$ at the photon energy $E_V = 1525\text{ eV}$ of the BTO peak with respect to the equilibrium value $I_{\text{XRD},0}$ at negative delays. We observe a maximum diffraction intensity drop of $\approx 4\%$ at $t = 3.5\text{ ps}$, with up to 99% recovery to the equilibrium value at $t \approx 7\text{ ps}$ (Figure 1c and Figure S5). We assign the initial 4% drop and recovery in diffraction intensity to the displacements of atoms within the BTO unit cell (inset of Figure 1c). Specifically, simulations based on the dynamical theory of diffraction (Figure S6) exclude the Debye-Waller effect and show that a decrease in the displacement $\Delta_{\text{Ti-O}}$ between the Ti atom and the center of the O octahedron by 8 pm can model the measured maximum change in peak diffraction intensity.

We focus next on the BTO (001) Bragg peak measured at longer time delays (Figure 1b). We observe that $I_{\text{XRD}}(E_V)$ at $t > 3\text{ ps}$ are shifted toward lower photon energies, i.e., larger out-of-plane lattice parameters c , with respect to $I_{\text{XRD}}(E_V)$ at smaller delays t . This can be clearly seen from the plot of the BTO out-of-plane strain $\bar{\eta}(t)$, averaged over d_{BTO} (Figure 1d). Here, $\bar{\eta}(t) = [c(t) - c_0]/c_0$, with $c(t)$ and c_0 representing the average \bar{c} at a given $t > 0\text{ ps}$ and $t \leq 0\text{ ps}$, respectively (see Methods). In Figure 1d, we find that: (i) the maximum compression of -0.024% occurs at $t = 2.6\text{ ps}$, (ii) $\bar{\eta}(t)$ increases linearly at a rate of $0.04\%/ps$ in the range $4\text{ ps} < t < 10\text{ ps}$, and (iii) settles at 0.34% at $\approx 20\text{ ps}$.

The model fitting $\bar{\eta}(t)$ data in Figure 1d is presented in the following. When a photon with energy $E > E_g$ is absorbed in BTO, electrons are photoexcited from the O 2p-derived valence band to the Ti 3d-derived conduction band^{29–31}. The thermalization of photoexcited electrons leads to an increase in the electron temperature (T_e), and to changes in the electronic system that can be modeled by the variation of the bandgap as a function of the electronic pressure $(\partial E_g/\partial p)$ ⁴. In turn, a modified

electron system affects the interatomic potential, resulting in atomic motions and contributing to the deformation potential stress $\sigma_{DP}(T_e, \partial E_g / \partial p)$. Subsequently, photoexcited electrons transfer part of their excess energy ($E - E_g$) to the phonon system via electron-phonon scattering, increasing the phonon temperature (T_p) on the picosecond timescale. This, in turn, induces a lattice expansion dependent on the BTO linear expansion coefficient (β), and contributes to the thermoelastic stress $\sigma_{TE}(T_p, \beta)$. The total stress^{4,32} $\sigma = \rho v^2 \eta + \sigma_{DP} + \sigma_{TE}$ generates a strain wave $\eta(z, t)$ that propagates through the material of mass density ρ at the longitudinal speed of sound v . We solve analytically the two-temperature model (Supplementary Note 7) and the lattice strain wave equation (Supplementary Note 8) to obtain $\eta(z, t)$. Finally, we calculate the strain $\bar{\eta}(t)$, averaged over d_{BTO} , to fit the experimental data in Figure 1d. The main outcome of our fit model is a negative $\partial E_g / \partial p$ of the order of $\approx 10^{-31} \text{ JPa}^{-1}$, in agreement with first-principles calculations³³, with a resulting bandgap decrease of about 3.2 meV (Supplementary Note 10). The negative $\partial E_g / \partial p$ causes lattice compression within the first ≈ 3 ps, when σ_{DP} dominates over σ_{TE} (inset of Figure 1d). Conversely, at larger time delays ($t > 3$ ps), T_p increases (Figure S17b) and the thermoelastic term becomes the dominant one, leading to lattice expansion (Figure S23).

Photoinduced ferroelectric polarization and electron dynamics

We turn now to investigating the dynamics of the ferroelectric polarization P_s and of the photoexcited carriers^{34–38}, upon excitation of the BTO film by the same 266 nm pump laser with fluence 2.7 mJ cm^{-2} . Therefore, we perform tr-SHG experiments^{27,39} and simultaneously tr-refl in reflection geometry (Figure 2a). From SHG polarimetry, i.e., the dependence of SHG intensity $I_{\text{SHG}}(\varphi) \propto |\chi_{ijk}^{(2)} E(\omega)^2|^2$ on the polarization angle of the probe beam φ , we learn about the optical tensor elements $\chi_{ijk}^{(2)}$ of a material, and thus its symmetry³⁹. By selecting either horizontal (p) or vertical (s) polarization of the SHG beam, we measure $I_{\text{SHG}}^p(\varphi)$ and $I_{\text{SHG}}^s(\varphi)$, shown in Figures 2b and c (blue points) together with the respective fit curves (see Methods), which are based on the 4mm point group symmetry with the following nonzero tensor elements: $\chi_{zxx}^{(2)}$, $\chi_{xxz}^{(2)}$, and $\chi_{zzz}^{(2)}$.

We observe a reduction of the BTO tetragonality, upon laser excitation, from the time evolution of $\chi_{zxx}^{(2)}$, $\chi_{xxz}^{(2)}$, and $\chi_{zzz}^{(2)}$ in the delay range $-1 \text{ ps} < t < 30 \text{ ps}$. While the 4mm symmetry is preserved also after the pump excitation (orange points in Figures 2b-c), a laser-induced change in tetragonality is observed. To visualize it, we display the relative change $\Delta\chi/\chi_0$ of $\chi_{xxz}^{(2)}$, $\chi_{zxx}^{(2)}$, and $\chi_{zzz}^{(2)}$ as a function of delay t (Figure 2d for $-1 \text{ ps} < t < 3 \text{ ps}$ and Figure S13 for $-1 \text{ ps} < t < 30 \text{ ps}$). The three tensor elements show similar dynamics, characterized by a fast fall time with the maximum drop after $\approx 500 \text{ fs}$ and two exponential recovery time constants of $\approx 5.5 \text{ ps}$ and $\approx 45 \text{ ps}$. Interestingly, the tensor elements representative of the electric dipole along the out-of-plane direction z ($\chi_{zxx}^{(2)}$ and $\chi_{zzz}^{(2)}$) show a nearly identical time dependence and a larger relative change than $\chi_{xxz}^{(2)}$, which refers to the in-plane electric dipole along the direction x . The difference between $\chi_{zxx}^{(2)}$ (or $\chi_{zzz}^{(2)}$) and $\chi_{xxz}^{(2)}$ reaches 0.5% after $\approx 500 \text{ fs}$ and decreases in a few tens of picoseconds (Figure S13). A purely thermal effect⁴⁰ would cause a uniform change of all tensor elements $\chi_{ijk}^{(2)}$, whereas the measured different dynamics of $\chi_{ijk}^{(2)}$ indicates a time-dependent lattice distortion of non-thermal origin. In fact, TD-DFT calculations^{29,30} show that upon charge transfer, the Ti-O_{||} bonds between Ti and apical O_{||} atoms (parallel to P_s) are weakened more than Ti-O_⊥ bonds between Ti and basal O_⊥ atoms (perpendicular to P_s), with a resulting reduction of the tetragonal distortion (inset of Figure 2d). Consequently, it is intuitive to expect a larger

amplitude of the induced electric dipole along the Ti-O_{||} direction (z) with respect to the Ti-O_⊥ direction (in the xy plane), as experimentally demonstrated by our data.

The proportionality $I_{\text{SHG}} \propto |\chi_{ijk}^{(2)}|^2 \propto |P_s|^2$ gives direct access to the magnitude of the spontaneous polarization³⁹. To this end, we measure the relative change $\Delta I_{\text{SHG}}^p / I_{\text{SHG},0}^p$ as a function of pump-probe delay t (Figure 2e), with the polarization of the 800 nm probe beam fixed to the maximum of $I_{\text{SHG}}^p(\varphi)$ at $\varphi = 0^\circ$ (Figure 2b). Simultaneously, we measure the relative change in reflectivity $\Delta R/R_0$ as a function of pump-probe delay t (Figure 2f). The data in Figure 2e [f] are well reproduced by a fit function consisting of the sum of three exponential decay terms, with fall [rise] time τ_0 , and recovery times τ_1 and τ_2 , convoluted with a Gaussian function representing the experimental temporal resolution (Supplementary Note 2). The initial drop in SHG intensity by 10% within 350 fs is followed by $\tau_1^{\text{SHG}} = 7.2(5)$ ps and $\tau_2^{\text{SHG}} = 200(140)$ ps recovery times, resulting in a 2.3% drop at 40 ps (Figure 2e). At the same time, we observe a fast increase in reflectivity by 7% within 350 fs, followed by two recovery times, $\tau_1^R = 5.2(1)$ ps and $\tau_2^R = 29.8(5)$ ps (Figure 2f).

In both tr-SHG and tr-refl data, the time needed to reach the maximum relative change (350 fs) might be due to the thermalization of photoexcited electrons via electron-electron scattering. Subsequently, thermalized electrons, which are higher in the conduction band, move to the bottom of the conduction band, transferring energy to the phonon system, and recombining with holes in the valence band via electron-phonon scattering^{4,37,41} or radiatively⁴². These processes are characterized by the recovery times τ_1 and τ_2 . Both τ_1 and τ_2 recovery constants of $\Delta I_{\text{SHG}}^p / I_{\text{SHG},0}^p$ are larger than those of $\Delta R/R_0$ because the dynamics of the spontaneous polarization results from the convolution of the faster dynamics of photoexcited carriers (seen by tr-refl) and the slower dynamics of atoms.

To interpret the SHG intensity drop and the reflectivity increase, it is useful to express the spontaneous polarization as^{22,43}: $P_s(t) = 1/V \sum_i q_i(t) \Delta z_i(t)$, where V is the volume of the unit cell, $q_i(t)$ is the Born effective charge and $\Delta z_i(t)$ is the out-of-plane displacement of atom i . The above-bandgap photoexcitation transfers electrons from the O 2p-derived valence band to the Ti 3d-derived conduction band of BTO. This charge transfer from O to Ti atoms reduces the corresponding charges q_i . We attribute changes in R to changes in photoexcited carrier density n_e ³⁵⁻³⁷, thus contributing to q_i , while P_s results from changes in both q_i and Δz_i . After 350 fs, before atomic movements can occur, the increase in carrier density n_e is responsible for the measured decrease in P_s and increase in R , shown in Figures 2e-f. This interpretation is corroborated by the increase of the maximum relative change of both $\Delta I_{\text{SHG}}^p / I_{\text{SHG},0}^p$ and $\Delta R/R_0$ with pump fluence (Figure S14 and Figure S15).

Discussion

We present here a unified picture in five stages of the lattice, polarization, and electron dynamics data presented above. Our observations are summarized in Figures 3a-e, and the physical mechanisms involved are sketched in Figures 3f-h. Before the arrival of the pump laser, the BTO is characterized by an out-of-plane polarization with given Born effective charges at each atomic site (stage 1, Figure 3a). Upon absorption of the pump laser at $t = 0$ ps, electrons move from the occupied O-derived valence band to the unoccupied Ti-derived conduction band (Figure 3f). Within ≈ 350 fs we observe the maximum increase in the photoexcited carrier density n_e , as indicated by the increase in $\Delta R/R_0$. This charge transfer reduces the Born effective charges q_i at Ti and O atoms, thereby decreasing the spontaneous polarization P_s , as indicated by the decrease in $\Delta I_{\text{SHG}}^p/I_{\text{SHG},0}^p$ (stage 2, Figure 3b). A smaller P_s is also consistent with a larger screening of long-range Coulomb interactions, which favor off-center atomic displacements and thus are responsible for the polar order. This effect is modeled by DFT calculations^{44,45}, showing that an increase in photoexcited carriers in the conduction band of BTO indeed tends to induce a phase transition from the ferroelectric to the paraelectric phase. Moreover, TD-DFT calculations^{29,30} predict that such photoinduced change of BTO electronic structure weakens more significantly Ti-O_{||} bonds, parallel to P_s , as compared to Ti-O_⊥ bonds, perpendicular to P_s . We demonstrate this effect experimentally by measuring a larger change of the out-of-plane tensor elements (χ_{xx} , χ_{zz}) as compared to the in-plane tensor element (χ_{xz}). In stage 2, in contrast to the maximum change in carrier density n_e and polarization P_s , the lattice remains unperturbed: this marks the onset of the decoupling between polarization and strain. At these early time delays, the bulk photovoltaic effect (BPVE)¹² and the Schottky interface effect¹¹ could potentially play a role, but we explain in the following why they are not dominant in our experiments.

First, in photoexcited ferroelectric materials it is common to observe the BPVE, i.e., the generation of photovoltage under light illumination^{46–48}. The BPVE occurs under two conditions: the presence of a noncentrosymmetrical crystal and the excitation of nonthermalized electrons⁴⁶. In our system both conditions are satisfied shortly after $t = 0$ ps, i.e., before hot electron thermalization takes place (Figure 3f). In BTO, if the light polarization is perpendicular to the spontaneous polarization P_s , the induced photovoltage is parallel to P_s ^{49,50}. This enhances P_s and induces, via the inverse piezoelectric effect, lattice expansion, similarly to what was observed in BiFeO₃⁵¹. However, in our study, although the polarization of the pump laser is perpendicular to P_s (Figure 2a), within ≈ 350 fs, when electrons are non-thermal and BPVE could potentially play a role, we see a decrease in P_s (Figure 2e). Hence, we conclude that BPVE is not a dominant effect in our experiments. In fact, this observation can be explained by the wavelength dependence of the BPVE, which shows a maximum when the photon energy is close to E_g , as observed, e.g., in Refs.^{12,52}. In contrast, in BTO at $\lambda = 266$ nm the contribution of BPVE is negligible, as observed in experiments^{49,50} and calculations⁴⁷.

Second, ferroelectric thin films grown on a metal substrate form a Schottky interface, where the electron-hole pairs generated by light absorption are separated by the built-in voltage of the Schottky barrier and cause a power-independent enhancement of the polarization for P_s pointing up (toward the surface)¹¹. This effect can be excluded as responsible for our experimental observations because: (i) although our sample has P_s pointing up (Figure S3), we see a decrease in P_s , and (ii) the

measured change in P_s linearly depends on the incident fluence (Figure S14). In fact, the Schottky interface effect is expected to play a significant role for films of thickness ≈ 10 nm or thinner¹¹, and to be negligible in our case due to the three-fold greater film thickness.

In the 350 fs – 3.5 ps delay range (stage 3, Figure 3c), we observe polarization and strain following opposite trends. In fact, while the displacement between Ti and the center of the O octahedron as well as the strain decreases, P_s starts to increase. This is attributed to the initial recombination of photoexcited carriers, suggested by the incipient recovery in $\Delta R/R$. At this stage, we also observe lattice compression caused by the negative parameter $\partial E_g/\partial p$ via the deformation potential. Our observation is in line with theory^{30,45,53} predicting a reduced bandgap E_g due to the presence of photoinduced carrier density (Figure 3g). Moreover, lattice contraction via the inverse piezoelectric effect is also consistent with an overall reduced P_s caused by photoexcited carriers⁵⁴.

In the 3.5 – 7 ps delay range (stage 4, Figure 3d), the relative displacement between Ti and O atoms tends to restore the ground state with a larger P_s . At the same time, the relaxation of photocarriers to the top of the conduction band and their recombination result in a further increase of the Born effective charges, and an energy transfer to the phonon temperature (Figure 3g), which, in turn, leads to lattice expansion. The latter effects persist up to $t \approx 20$ ps.

At $t \approx 20$ ps (stage 5, Figure 3e), together with a further relaxation of the electronic system toward equilibrium, we observe a saturation of the BTO average strain. This results in a metastable state with a slightly reduced P_s and a significantly increased out-of-plane strain with respect to the ground state. The reduced P_s is attributed to the presence of residual photoexcited carriers in the conduction band (Figure 3h), while the increased out-of-plane strain is due to the thermoelastic contribution. We exclude the depolarization field screening as the main driving effect for the transient tensile strain seen in our experiments, because it would lead to the typical saturation of the strain with increasing pump fluence⁵⁵. For example, in PbTiO_3 ¹² the metastable lattice strain reaches saturation with 266 nm laser fluences of 0.01 mJ cm^{-2} . Conversely, in our study, we employ two orders of magnitude larger pump fluence and still the metastable strain scales approximately linearly with the pump fluence (Figure 1d and Figure S18). In addition, on the ≈ 20 ps timescale, the deformation potential plays a minor role (Figure S23), thus its influence on the bandgap is expected to be marginal. Interestingly, although the out-of-plane lattice parameter is larger than in the ground state (c_0), the polarization P_s is still smaller compared to equilibrium. This underscores the persistence of the decoupling between polarization and strain. Quantitatively, we estimate that in stage 5 the contribution of photoexcited electrons to P_s has $\approx 10\%$ larger magnitude than the structural contribution from the strain η (Supplementary Note 11).

In summary, we demonstrate that, with an above-bandgap laser excitation, an ultrafast decoupling of spontaneous polarization and strain can be achieved and measured. We assign this effect to the dominant contribution of photoexcited electrons in determining the spontaneous polarization when the system is out of equilibrium, and show that for an accurate description and fundamental understanding of a ferroelectric material in a photoexcited state, it is essential to combine multiple techniques that address the dynamical evolution of the various degrees of freedom, i.e., lattice, ferroelectric polarization, and electrons. The decoupling of polarization from the strain offers the opportunity to change paradigm from strain engineering⁵⁶

to light-induced polarization engineering, thereby lifting the constraint of selecting among a limited number of substrates²⁴ or designing freestanding membranes²⁶ to tune the spontaneous polarization. Moreover, by softening the Ti-O_{||} bonds, we bring BTO to an excited state, where it could be further modified by THz light to achieve stable and reversible polarization switching at lower fluences than otherwise needed when starting from the ground state²¹. Finally, the transient and reversible control of the spontaneous polarization, shown in this study, offers a pathway to control by light both electric and magnetic degrees of freedom in multiferroic materials.

Methods

Sample preparation and characterization

The epitaxial bilayers BTO/SRO were grown on a GSO substrate using pulsed laser deposition. The ceramic targets of SRO and BTO were 8 cm away from the substrate and ablated using a KrF excimer laser ($\lambda = 248\text{ nm}$, fluence 5.4 J cm^{-2} , 2 Hz repetition rate). The deposition of SRO and BTO layers was conducted in O_2 atmosphere with pressure $p_{\text{O}_2} = 100\text{ mTorr}$ and deposition temperatures of 908 K and 973 K, respectively. Sample cooling with the rate of 3 K min^{-1} was conducted in the environment of saturated O_2 ($p_{\text{O}_2} = 10^4\text{ mTorr}$) to prevent the formation of oxygen vacancies. The thicknesses of BTO and SRO layers, $d_{\text{BTO}} = 34.5\text{ nm}$ and $d_{\text{SRO}} = 47\text{ nm}$ are extracted from a θ - 2θ scan of the as-grown sample around the (002) reflections (Figure S1), while the GSO substrate is 0.5 mm thick. We determine the out-of-plane lattice parameters $c_{\text{BTO}} = 4.074\text{ \AA}$, $c_{\text{SRO}} = 3.934\text{ \AA}$, and $c_{\text{GSO}} = 3.964\text{ \AA}$ by means of the reciprocal space map shown in Figure S2. The in-plane lattice parameter $a = 3.970\text{ \AA}$, common to BTO, SRO and GSO, indicates that both BTO and SRO thin films are coherently strained to the substrate. Furthermore, the absence of satellite peaks in Figure S2 suggests the existence of a BTO monodomain. We determine that the spontaneous polarization of the as-grown sample P_s points upward (toward the surface) by means of piezoresponse force microscopy (Figure S3). The linear expansion coefficients of BTO above $T_c = 400^\circ\text{C}$, of SRO and GSO in the temperature range $35^\circ\text{C} < T < 700^\circ\text{C}$ are determined by θ - 2θ scans as a function of sample temperature (Figure S4).

Time-resolved X-ray diffraction

Time-resolved X-ray diffraction experiments were performed at the Spectroscopy and Coherent Scattering instrument (SCS) of the European X-Ray Free-Electron Laser Facility (EuXFEL), using an optical laser (OL) as pump and the XFEL as probe. The XFEL pulse pattern consisted of pulse trains at a repetition rate of 10 Hz, with 35 pulses per train at the intratrain repetition rate of 113 kHz. The full width at half maximum (FWHM) of the XFEL spectrum was 11.7 eV. To reduce the energy bandwidth, the XFEL beam was monochromatized using a variable line spacing grating with 50 lines/mm in the first diffraction order and exit slits with a gap of 100 μm , providing an energy resolution of $\approx 650\text{ meV}$. The nominal pulse duration of the XFEL pulses was $\approx 25\text{ fs}$, with pulse stretching at the monochromator grating of $\approx 10\text{ fs}$ (FWHM). The XFEL pulses, with initial energy of 1.5 mJ per pulse, were then attenuated by transmission through a gas attenuator (GATT), consisting of a volume containing N_2 gas at a variable pressure. In order to prevent detector saturation, the transmission of the GATT was set to have $\approx 15\text{ nJ}$ per pulse at the sample. The XFEL pulse energy was measured by an X-ray gas monitor detector (XGM), located $\approx 7\text{ m}$ upstream of the sample, just before the Kirkpatrick-Baez (KB) mirrors. The latter were used to focus the XFEL beam at the sample to a spot size of $w_x^{\text{XFEL}} \times w_y^{\text{XFEL}} = 140\text{ }\mu\text{m} \times 100\text{ }\mu\text{m}$ (determined by knife edge scans), where w is defined as the distance from the beam axis where the intensity drops to $1/e^2$ of the value on the beam axis. The angle of incidence (defined from the sample surface) of XFEL and OL beams at the sample was 86° and 85° , respectively. The intensity of each XFEL pulse diffracted by the sample was measured by a Si avalanche photodiode (APD, model SAR3000G1X, Laser Components), converted to a voltage pulse and digitized. To prevent the pump laser intensity from reaching the APD, the latter was equipped with a filter made of 400 nm Ti, deposited on 200 nm polyimide.

The pump laser had a central wavelength of 266 nm, the same pulse pattern as the XFEL with pulse duration of 70 fs, and beam size $w_x^{\text{OL}} \times w_y^{\text{OL}} = 330 \mu\text{m} \times 240 \mu\text{m}$, determined by knife edge scans. The transmittance profile of the 266 nm laser in our BTO/SRO/GSO sample is reported in [Supplementary Note 6.1](#). The incident pump laser fluence at the sample was 2.7 mJ cm^{-2} , and we verified that diffraction curves $I_{\text{XRD}}(E_V)$ measured at negative delays t coincide with those measured without the pump laser ([Figure S7](#)). This confirms the reversibility of the pump effect induced by UV laser light. The temporal overlap between XFEL and OL was determined as detailed in [Figure S8](#). The diffracted intensity of the XFEL pulses in a train was averaged and the corresponding time delay of the OL was corrected by the respective bunch arrival monitor (BAM) value, obtaining a time resolution $\Delta t \approx 90 \text{ fs}$ ([Supplementary Note 4](#)). Data measured with incident pump laser fluence of 1.4 mJ cm^{-2} are reported in [Supplementary Note 8](#) and [Supplementary Note 9](#).

In general, two kinds of tr-XRD experiments were performed: photon energy scans at a fixed pump-probe delays t ([Figure 1b](#) and [Figure S5](#)), and time delay scans at a fixed photon energy $E_V = 1525 \text{ eV}$ ([Figure 1c](#) and [Figure S8](#)). The energy scans were carried out by a simultaneous movement of the monochromator grating and the undulators gap, such to have always the peak of the XFEL spectrum at the desired photon energy. From the energy scans at different t , the out-of-plane lattice parameters $c(t)$ and c_0 are calculated as the center-of-mass of the BTO diffraction intensity $I_{\text{XRD}}(t)$ and refer to the average c over d_{BTO} (\bar{c}). Specifically, the BTO average out-of-plane parameters \bar{c} is calculated from the corresponding (001) Bragg peaks using the Bragg condition $\bar{c} = (12400 \text{ eV \AA}) / (2\bar{E}_V \sin \theta)$, where \bar{E}_V is the average of energy values, around the (001) BTO peak, weighted by $I_{\text{XRD}}(E_V)$. Energy scans at different pump-probe delays t over the photon energy range covering also GSO (001) and SRO (001) Bragg peaks are reported in [Figure S9](#).

Time-resolved SHG and reflectivity

Time-resolved Second Harmonic Generation and time-resolved reflectivity experiments were performed at the SCS instrument of the EuXFEL using the same optical laser employed for tr-XRD experiments and the same pulse pattern. A sketch of the setup is shown in [Figure 2a](#). The 800 nm probe beam at frequency ω (red arrow) impinges on the sample at angle $\theta = 50^\circ$ (defined from the normal to the surface) with polarization defined by the angle φ and varied by rotating a half waveplate. The angle $\varphi = 0^\circ$ [$\varphi = 90^\circ$] refers to p [s] polarized light. The 266 nm pump beam at frequency 3ω (purple arrow) impinges on the sample at normal incidence with p polarization. The 800 nm probe beam is then reflected by the sample and a dichroic mirror before reaching a Si photodiode. The latter is used to measure tr-refl of our sample. The 400 nm beam at frequency 2ω (blue arrow) is the SHG signal generated in the BTO sample ([Figure S11](#)). This SHG beam is transmitted through the dichroic mirror and Glan polarizer, which is set to select either the p or s component of the electric field, corresponding to the p -out or s -out configuration, respectively. Finally, the SHG beam is filtered by a 400 nm bandpass filter before reaching a photomultiplier (model H10721-210-Y004, Hamamatsu). The azimuthal rotation of the sample around the z axis is defined by the angle γ . The independence of both polar plots of $I_{\text{SHG}}^p(\varphi)$ and $I_{\text{SHG}}^s(\varphi)$ from γ confirms the out-of-plane nature of the spontaneous polarization of our BTO sample ([Figure S12](#)). Both Si photodiode and photomultiplier measure respectively the reflectivity and SHG signal of each OL pulse in the train. The pulse duration of the 800 nm probe and 266 nm pump beams

were approximately 50 fs and 70 fs, providing a time resolution of ≈ 90 fs. The beam sizes of 800 nm and 266 nm beams, determined by knife edge scans, were $w_x^{800\text{nm}} \times w_y^{800\text{nm}} = 55 \mu\text{m} \times 46 \mu\text{m}$ and $w_x^{266\text{nm}} \times w_y^{266\text{nm}} = 165 \mu\text{m} \times 311 \mu\text{m}$, respectively. The penetration depths of 800 nm, 400 nm and 266 nm laser beams in BTO are reported in [Supplementary Note 6.2](#). While the fluence of the 800 nm probe beam was kept at 1.3 mJ cm^{-2} , the fluence of the 266 nm pump beam was set to 2.7 mJ cm^{-2} for the data displayed in [Figure 2](#). tr-SHG and tr-refl data with fluences between 1.4 mJ cm^{-2} and 12.3 mJ cm^{-2} are reported in [Figure S14](#) and [Figure S15](#).

In general, given the incoming electric field with components $E_j(\omega)$ and $E_k(\omega)$ at frequency ω along j and k directions, the electric dipole polarization induced in the material at frequency 2ω along the direction i is $P_i(2\omega) = \chi_{ijk}^{(2)} E_j(\omega) E_k(\omega)$, where $\chi_{ijk}^{(2)}$ is the second-order susceptibility, i.e., a third rank tensor reflecting the symmetry of the material. Each direction i, j, k can be $x, y,$ or z directions ([Figure 2a](#)). By selecting p or s polarization of the SHG beam, we measure $I_{\text{SHG}}^p(\varphi)$ or $I_{\text{SHG}}^s(\varphi)$, which, for a BTO single crystal with 4mm point group symmetry, can be expressed as^{11,39}:

$$I_{\text{SHG}}^p(\varphi) \propto (\chi_{zxx} \sin \theta \cos \varphi^2 + (2\chi_{xxz} \cot \theta^2 + \chi_{zxx} \cot \theta^2 + \chi_{zzz}) \sin \theta^3 \sin \varphi^2)^2, \quad (1)$$

$$I_{\text{SHG}}^s(\varphi) \propto (2\chi_{xxz} \sin \theta \sin \varphi \cos \varphi)^2. \quad (2)$$

The resulting ratios of the tensor elements in [Figure 2b-c](#), $\chi_{zzz}^{(2)}/\chi_{zxx}^{(2)} = 3.7$ and $\chi_{zzz}^{(2)}/\chi_{xxz}^{(2)} = 6.5$, reflect a thin film under tensile out-of-plane stress⁵⁷. The good quality of the fit curves in [Figure 2b-c](#) confirms that our BTO thin film has 4mm point group symmetry. The minor discrepancies between data and fit model might be due to the fact that our BTO thin film is coherently strained to the substrate, and this leads to the appearance of additional minor nonzero tensor elements⁵⁸.

Data availability

Data recorded for the experiment at the European XFEL are available at doi:10.22003/XFEL.EU-DATA-003481-00. Source data are provided with this paper. Further experimental data as well as the simulation data that support the findings of this study are available from the corresponding author upon reasonable request.

Code availability

Codes generated during the current study are available from the corresponding author on reasonable request.

Acknowledgements

We acknowledge the European XFEL in Schenefeld, Germany, for provision of the XFEL beamtime at the SCS scientific instrument and would like to thank the staff for their assistance. D.P. acknowledges funding from 'la Caixa' Foundation fellowship (ID 100010434) and the Spanish Ministry of Industry, Economy and Competitiveness (MINECO), grant no PID2019-109931GB-I00. The ICN2 is funded by the CERCA programme/Generalitat de Catalunya and by the Severo Ochoa Centres of Excellence Programme, funded by the Spanish Research Agency (AEI, CEX2021-001214-S). T.C.A. acknowledges funding from the Heisenberg Resonant Inelastic X-ray Scattering (hRIXS) Consortium. We thank D. Hickin for support with the automation of tr-SHG measurements. We thank A. Reich and J.T. Delitz for the design of mechanical components used in tr-XRD experiments. We are grateful to M. Altarelli for careful reading of the manuscript.

Author contributions

G.Merc., with input from L.P.H., G.C., I.A.V., J.Z. and T.L.L., conceived the experiments. G.C. and I.S., with input from G.Merc., designed the sample. J.M.C.R. manufactured the sample and D.P. characterized it with θ - 2θ scan, RSM and PFM. L.P.H., D.P., G.N.H., R.C., L.M., M.T., S.G., T.C.A., G.Merz., S.P., J.Sc., Z.Y., I.A.V. and G.Merc. performed tr-XRD experiments. C.C. developed an online analysis tool to visualize tr-XRD data in real time. G.Merc. and L.P.H. performed tr-SHG and tr-refl experiments. J.Sa. performed θ - 2θ measurements at different sample temperatures. L.P.H. and G.Merc. analyzed all the data. L.P.H. modeled tr-XRD and tr-SHG data. G.Merc., A.S., K.R. and I.A.V. supervised the project. G.Merc. wrote the manuscript, drafted by L.P.H., and with input from all authors. All authors provided critical feedback and helped shape the research, analysis and manuscript.

Ethics declarations

The authors declare no competing interests.

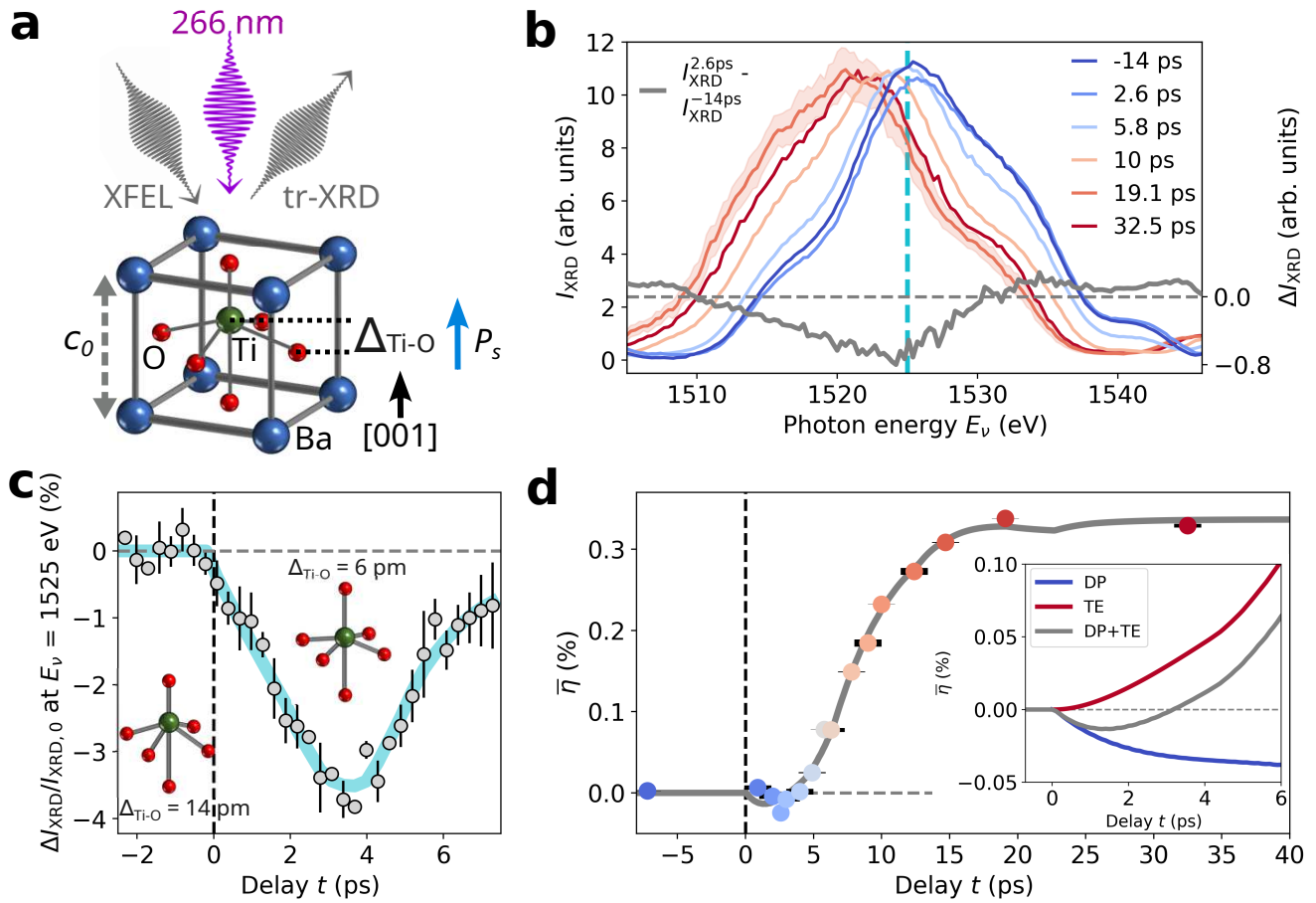


Figure 1. Photoinduced structural dynamics and time evolution of strain. (a) Sketch of the BaTiO_3 unit cell, the out-of-plane lattice parameter in the ground state c_0 , the relative displacement $\Delta_{\text{Ti-O}}$ of the Ti atom from the center of the O octahedron, the spontaneous ferroelectric polarization P_s , the pump laser at 266 nm, the incident and diffracted XFEL beams. (b) Selected experimental $I_{\text{XRD}}(E_\nu)$ curves at different time delays t , and the difference $\Delta I_{\text{XRD}} = I_{\text{XRD}}^{2.6\text{ps}} - I_{\text{XRD}}^{-14\text{ps}}$ (gray line). The vertical dashed cyan line marks $E_\nu = 1525$ eV. The shaded red area indicates the standard deviation value $\text{SD} \approx 0.1 \times I_{\text{XRD}}^{19.1\text{ps}}$, with similar values also for the diffraction curves at different delays t . For clarity, only the error bar of $I_{\text{XRD}}^{19.1\text{ps}}$ is shown. (c) Delay dependence of $\Delta I_{\text{XRD}}/I_{\text{XRD},0} = [I_{\text{XRD}}(t) - I_{\text{XRD},0}]/I_{\text{XRD},0}$, i.e., the relative change of $I_{\text{XRD}}(t)$ at the photon energy $E_\nu = 1525$ eV with respect to the equilibrium value at negative delays $I_{\text{XRD},0}$. The solid cyan line is a guide to the eye. The error bars indicate the standard deviation of experimental data in a bin size of 300 fs. Inset: sketch of Ti and O octahedron at negative delays ($\Delta_{\text{Ti-O}} = 14$ pm), and at 3.5 ps ($\Delta_{\text{Ti-O}} = 6$ pm). (d) Average BTO out-of-plane strain $\bar{\eta}(t)$ as a function of pump-probe delay t . The error bars follow from the determination of c from $I_{\text{XRD}}(E_\nu) \pm \text{SD}$. The solid gray line is a fit to the data (Supplementary Note 8). Inset: Modeled contributions to the average strain $\bar{\eta}(t)$ due to deformation potential (DP) and thermoelastic (TE) stress (Figure S23).

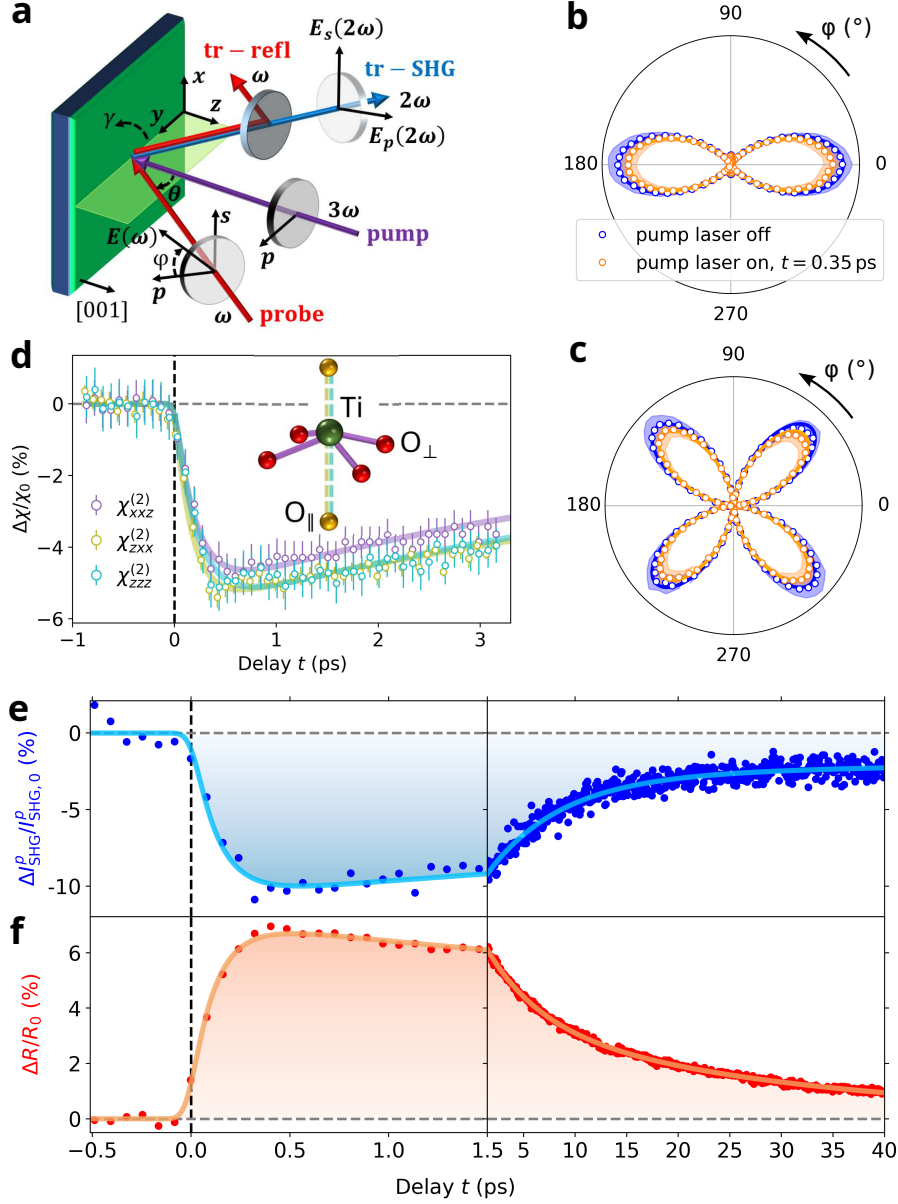


Figure 2. Photoinduced ferroelectric polarization and electron dynamics. (a) Sketch of the tr-SHG and tr-refl setup. Polar plots of $I_{\text{SHG}}^p(\varphi)$ (b) and $I_{\text{SHG}}^s(\varphi)$ (c) measured without pump laser (blue points) and with pump laser at the delay $t = 0.35$ ps (orange points). The green solid lines are fit curves to the data resulting from equations (1) and (2). The shaded orange and blue areas refer to the standard deviation of the data and amount to $\approx 13\%$. (d) Relative change $\Delta\chi/\chi_0$ of the tensor elements $\chi_{xxz}^{(2)}$, $\chi_{zxx}^{(2)}$, and $\chi_{zzz}^{(2)}$ as a function of delay t , and respective fit curves (Supplementary Note 2). $\Delta\chi/\chi_0 = (\chi_{ijk}^{(2)} - \chi_{ijk,0}^{(2)})/\chi_{ijk,0}^{(2)}$, where $\chi_{ijk,0}^{(2)}$ refers to the tensor element $\chi_{ijk}^{(2)}$ at $t \leq 0$ ps. The error bars refer to the standard deviation resulting from the fit of the tensor elements. Inset: sketch of Ti atom and O octahedron with the indication of O_{\parallel} (yellow spheres) and O_{\perp} (red spheres), and the softening of Ti- O_{\parallel} bonds (dashed olive and cyan lines) with respect to the Ti- O_{\perp} bonds (solid purple lines). Relative change of SHG $\Delta I_{\text{SHG}}^p/I_{\text{SHG},0}^p$ (e) and reflectivity $\Delta R/R_0$ (f) as a function of the delay t . $\Delta I_{\text{SHG}}^p/I_{\text{SHG},0}^p = [I_{\text{SHG}}^p(t) - I_{\text{SHG},0}^p]/I_{\text{SHG},0}^p$, where $I_{\text{SHG},0}^p$ refers to the SHG intensity at $t \leq 0$ ps. $\Delta R/R_0 = [R(t) - R_0]/R_0$, where R_0 refers to the reflectivity at $t \leq 0$ ps. The solid lines are fit curves to the data with fit parameters τ_0 , τ_1 , and τ_2 reported in the text. The error bar of $\Delta I_{\text{SHG}}^p/I_{\text{SHG},0}^p$ and $\Delta R/R_0$ data points are $\approx 8\%$ and 2% , respectively. Since SHG is a nonlinear process, it is more significantly affected by fluctuations of the 800 nm probe laser intensity of $\approx 2\%$. However, the standard deviation of $\Delta I_{\text{SHG}}^p/I_{\text{SHG},0}^p$ and $\Delta R/R_0$ at $t < 0$ ps are 0.6% and 0.06% , respectively.

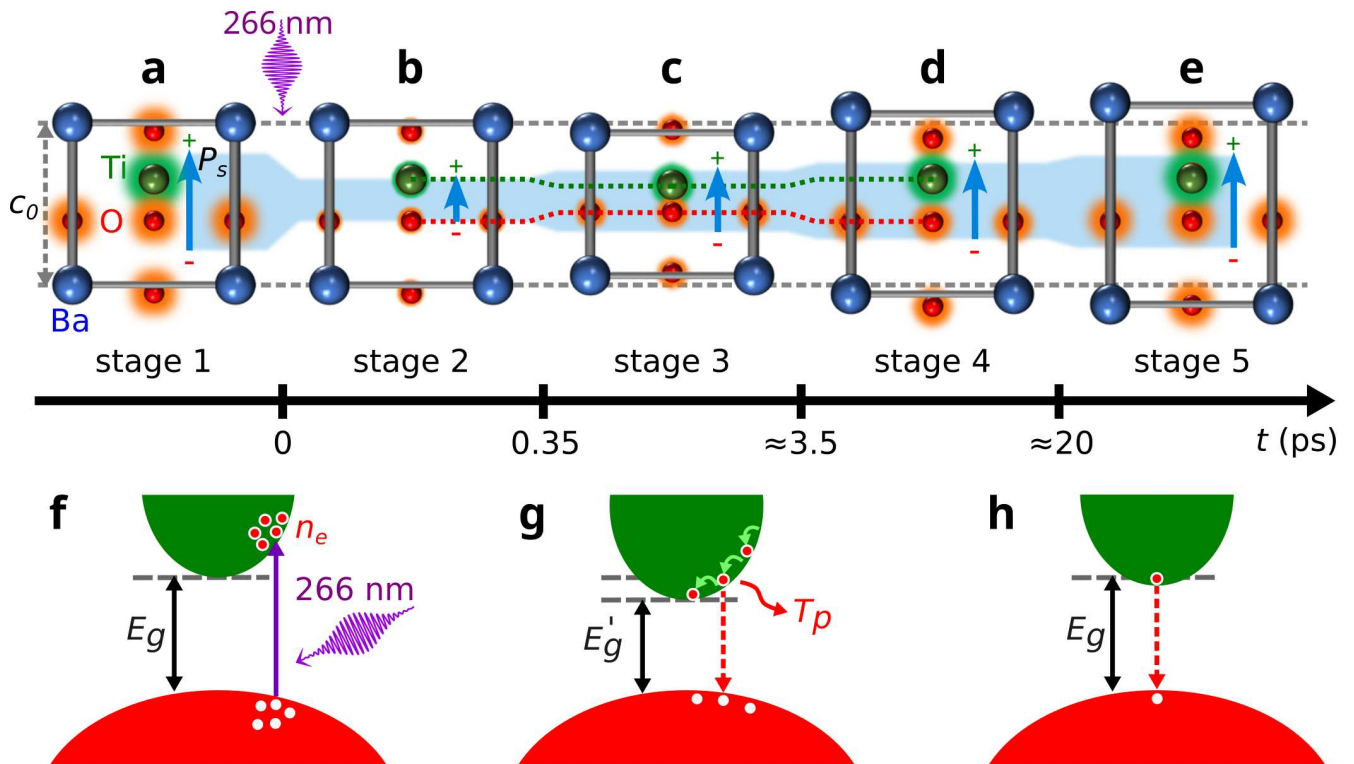


Figure 3. Schematic model of photoinduced lattice structure, polarization and electron dynamics. BTO unit cell, projected along the [100] direction, at the following time delays t : $t < 0$ ps, i.e., ground state (a), $0 \text{ ps} < t < 0.35$ ps (b), $0.35 \text{ ps} < t < 3.5$ ps (c), $3.5 \text{ ps} < t < 20$ ps (d), $\gtrsim 20$ ps (e). The distance between the horizontal dashed gray lines indicates the out-of-plane lattice parameter at equilibrium c_0 in panels (a)-(e). The size of the green and red shaded areas around Ti and O atoms, are proportional to the corresponding positive and negative Born effective charges, respectively. For clarity, the Born effective charge of Ba atoms is omitted. The length of the light blue arrow and the height of the blue shaded area are proportional to the magnitude of the spontaneous polarization P_s . Sketch of BTO valence and conduction band in stage 2 (f), in stages 3 and 4 (g), and in stage 5 (h). The purple vertical arrow indicates the photoexcitation of electrons from the valence to the conduction band upon absorption of a 266 nm laser photon. $E_g = 3.4 \text{ eV}$ is the bandgap of the ground state, E'_g is the bandgap of the excited state, modified by the deformation potential, with $E'_g - E_g \approx -3.2 \text{ meV}$ (Supplementary Note 10). The relaxation of the hot electrons to the bottom of the conduction band (green arrows) and the recombination with holes of the valence band (red dashed vertical arrow) induce an increase of T_p . Panel (h) indicates the minor contribution of the deformation potential, resulting in a bandgap close to E_g , and the residual presence of electrons in the conduction band.

Supplementary Information for:

Ultrafast decoupling of polarization and strain in ferroelectric BaTiO₃

Supplementary Note 1 Sample characterization

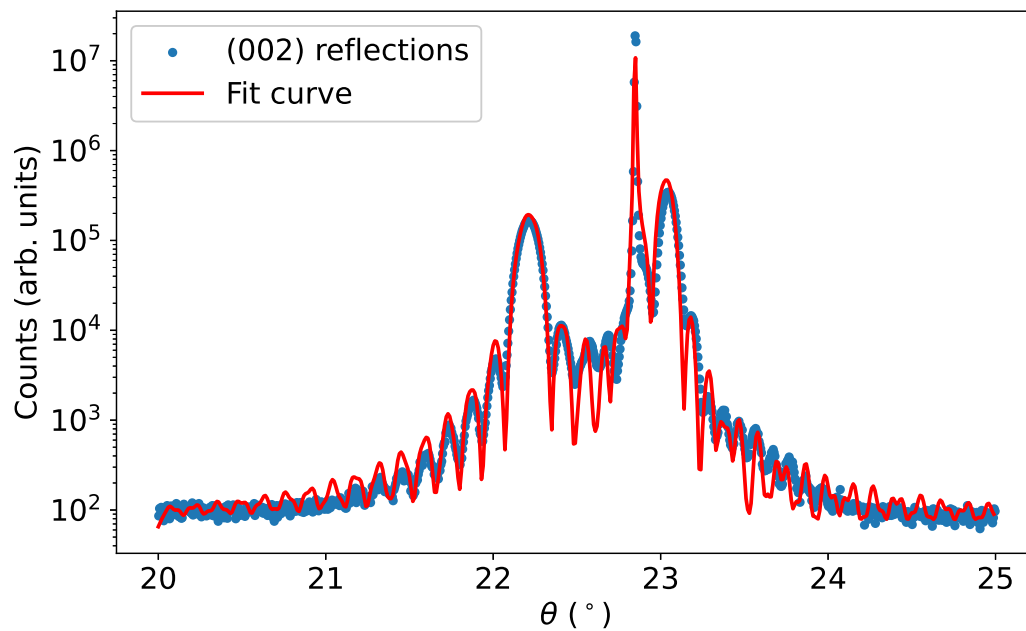


Figure S1. θ - 2θ scan. θ - 2θ scan of the as-grown sample around the (002) reflections of BTO and SRO thin films, and the GSO substrate. The measurements are performed using a PANalytical X'Pert Pro diffractometer, and the experimental data are modeled by the dynamical theory of diffraction with BTO and SRO thicknesses as fit parameters, providing $d_{\text{BTO}} = 34.5$ nm and $d_{\text{SRO}} = 47$ nm, respectively.

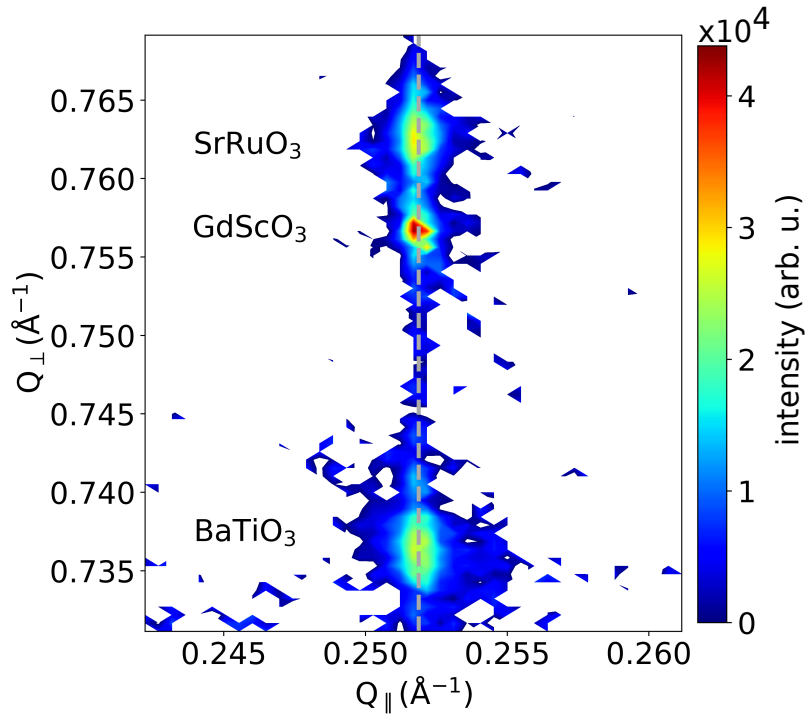


Figure S2. Reciprocal space map. X-ray reciprocal space map (RSM) of the sample around the $(\bar{1}03)$ substrate Bragg peak, measured by a PANalytical X'Pert Pro diffractometer. The vertical gray dashed line indicates the reciprocal lattice parameter Q_{\parallel} shared by the GSO substrate, BTO, and SRO thin films. The reciprocal lattice parameters Q_{\parallel} and Q_{\perp} of the intensity peaks are related to the real space in-plane a and out-of-plane c lattice parameters by the following relations⁵⁹: $a = Q_{\parallel}^{-1} = -\lambda/(2Q_x)$ and $c = (Q_{\perp}/3)^{-1} = (3\lambda)/(2Q_z)$. Here, $\lambda = 1.5406 \text{ \AA}$ is the wavelength of the incident $\text{Cu } K\alpha$ radiation, $Q_x = \sin(\theta) \sin(\theta - \omega)$, and $Q_z = \sin(\theta) \cos(\theta - \omega)$, where 2θ is the angle between incident and outgoing wavevector, and ω is the angle between incident wavevector and sample surface. Fitting the RSM intensity distribution with a pseudo-Voigt function⁶⁰ provides Q_{\parallel} and Q_{\perp} of each diffraction peak, and the following lattice parameters: $a = 3.970 \text{ \AA}$, $c_{\text{BTO}} = 4.074 \text{ \AA}$, $c_{\text{SRO}} = 3.934 \text{ \AA}$, and $c_{\text{GSO}} = 3.964 \text{ \AA}$.

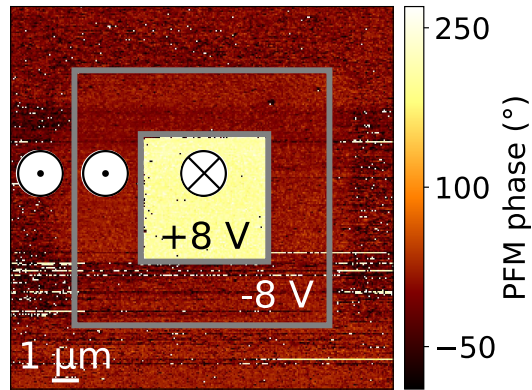


Figure S3. Piezoresponse force microscopy. Piezoresponse force microscopy (PFM) phase image of the BTO/SRO/GSO sample. Piezoresponse force microscopy in Dual AC Resonance Tracking (DART) mode⁶¹ is used to probe the polarization of as-grown samples and to prove that ferroelectric polarization can be switched by the application of positive or negative voltage between the PFM tip and the SRO electrode. The application of tip voltage 8 V [−8 V], to the regions marked by the gray boxes, forces a downward [upward] polarization P_s pointing away from the surface (⊗) [toward the surface (⊙)], with the corresponding PFM phase 180° [0°]. The PFM phase in the region where no voltage is applied (beyond the outer gray box) reveals that our as-grown sample has upward polarization P_s with no indication of multiple domains.

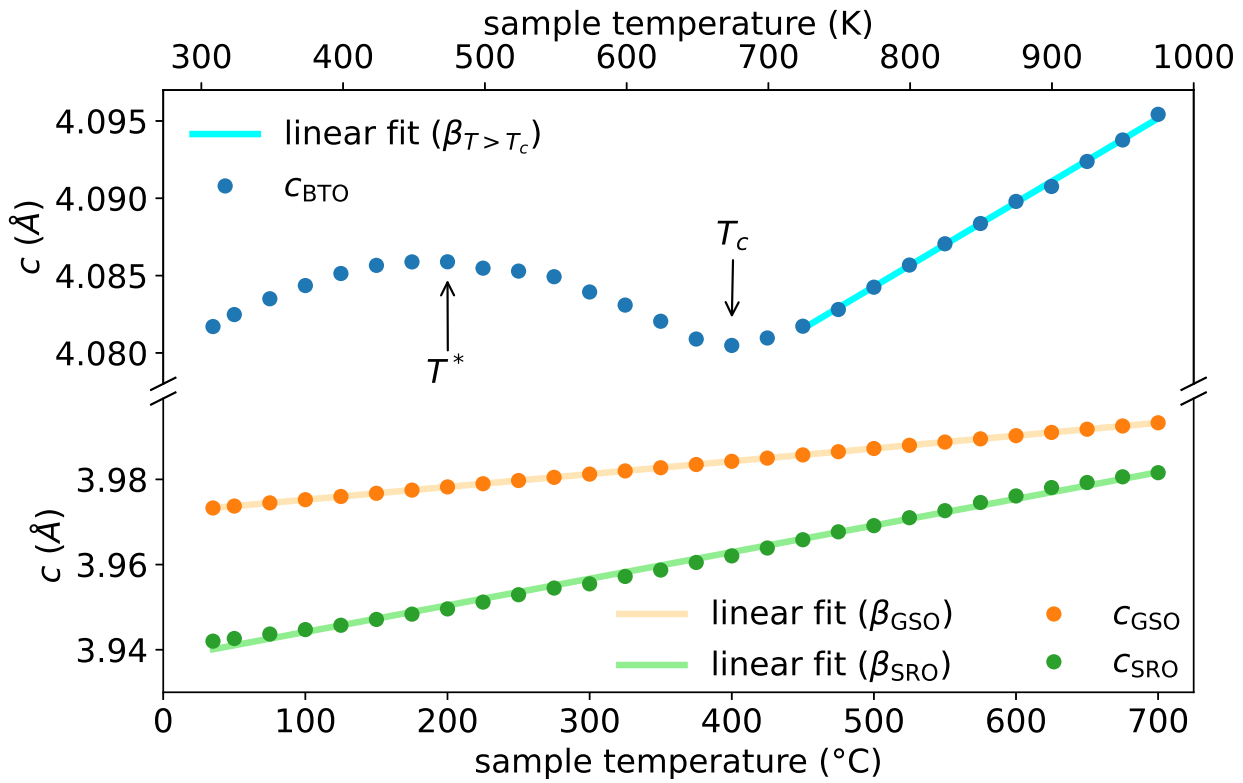


Figure S4. c parameters as a function of sample temperature. Out-of-plane lattice constant c of BTO (blue points), SRO (green points), and GSO (orange points) as a function of the sample temperature. The c parameters are extracted from θ - 2θ scans (similar to Figure S1) measured at different sample temperatures. The arrows indicate $T^* = 200^\circ\text{C}$ and $T_c = 400^\circ\text{C}$. The blue line is a linear fit of c_{BTO} data that provides $\beta_{T>T_c} = 1.33 \times 10^{-5} \text{K}^{-1}$. The orange and green lines are linear fits of c_{GSO} and c_{SRO} data, which provide $\beta_{\text{GSO}} = 7.6 \times 10^{-6} \text{K}^{-1}$ and $\beta_{\text{SRO}} = 1.58 \times 10^{-5} \text{K}^{-1}$, respectively.

Supplementary Note 2 Fit function of tr-XRD, tr-SHG and tr-refl delay scans

The function used to fit the delay scans presented in this work is:

$$F(t) = h(t) * g(t). \quad (\text{S1})$$

Equation (S1) is the convolution of the sum of three exponential decays $h(t) = \sum_{i=1}^3 A_i \exp(- (t - t_0)/\tau_i)$, with the Gaussian function $g(t) = \sqrt{2}/(\sigma\sqrt{\pi}) \exp(- (t - t_0)^2/(2\sigma^2))$, where $\sigma = \Delta t/(2\sqrt{2\ln 2})$ and Δt is the time resolution (FWHM) of our experiment (Supplementary Note 4). The resulting fit function can be written as:

$$F(t) = \sum_{i=1}^3 A_i \exp\left(\frac{\sigma^2}{2\tau_i^2} - \frac{t - t_0}{\tau_i}\right) \left(1 - \operatorname{erf}\left(\frac{\sigma^2 - \tau_i(t - t_0)}{\sqrt{2}\sigma\tau_i}\right)\right), \quad (\text{S2})$$

with the time constants t_0 , τ_1 , τ_2 , and τ_3 and the amplitudes A_1 , A_2 , and A_3 as fit parameters.

Supplementary Note 3 XRD data

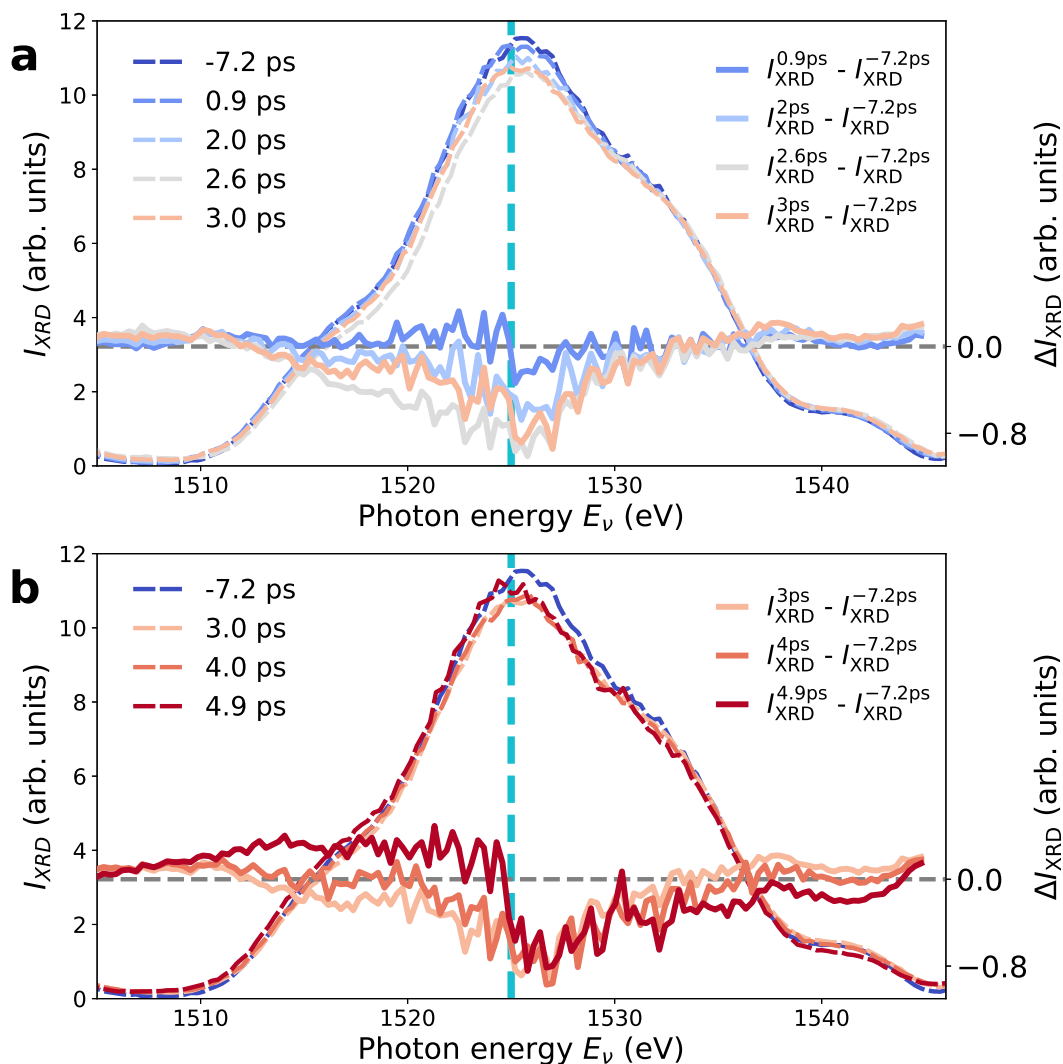


Figure S5. Diffraction intensity drop. Experimental $I_{\text{XRD}}(E_{\nu})$ curves at different pump-probe delays t , and the respective differences $\Delta I_{\text{XRD}} = I_{\text{XRD}}^t - I_{\text{XRD}}^{-7.2\text{ps}}$, where $t = 0.9\text{ps}, 2\text{ps}, 2.6\text{ps}, 3\text{ps}, 4\text{ps}, 4.9\text{ps}$. The vertical dashed cyan line marks $E_{\nu} = 1525\text{eV}$. These data highlight that up to $\approx 3 - 4\text{ps}$ there is mostly a drop in diffraction intensity near the peak center, accompanied by a minor shift of the spectral weight to higher photon energies ($I_{\text{XRD}}^{2.6\text{ps}}$), indicating lattice compression. After 4 ps the diffraction intensity near the peak center increases and the peak shifts to the lower photon energies ($I_{\text{XRD}}^{4.9\text{ps}}$), indicating lattice expansion.

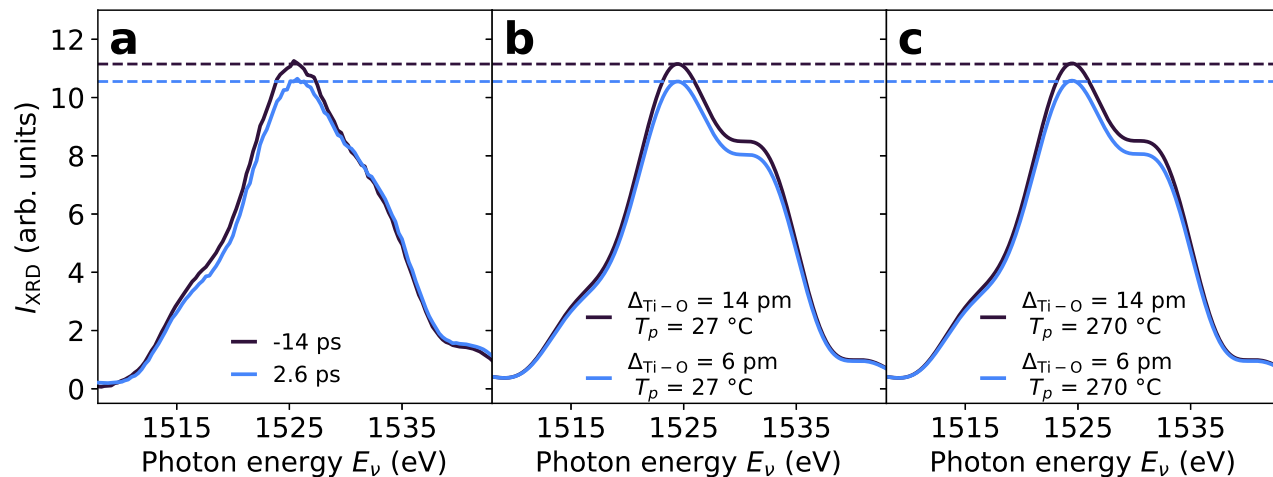


Figure S6. Contribution of Debye-Waller factor. (a) BTO (001) diffraction peak measured at $t = -14$ ps and $t = 2.6$ ps (same as in Figure 1b). Diffraction intensity simulations that mimic the drop of peak diffraction intensity with $\Delta_{\text{Ti-O}} = 14$ pm and $\Delta_{\text{Ti-O}} = 6$ pm at $T_p = 27^\circ\text{C}$ (b) and $T_p = 270^\circ\text{C}$ (c). The minimal difference between the diffraction curves in panels (b) and (c) shows that the effect of the average lattice temperature T_p on the diffraction intensity, via the Debye-Waller effect, is negligible in the T_p range relevant to this work ($T_p \leq 270^\circ\text{C}$, Figure S17b). Moreover, the non-monotonic decrease and increase in peak diffraction intensity in the region $0 \text{ ps} < t < 7 \text{ ps}$ is not consistent with the monotonic increase of T_p upon absorption of the pump laser (Figure S17b).

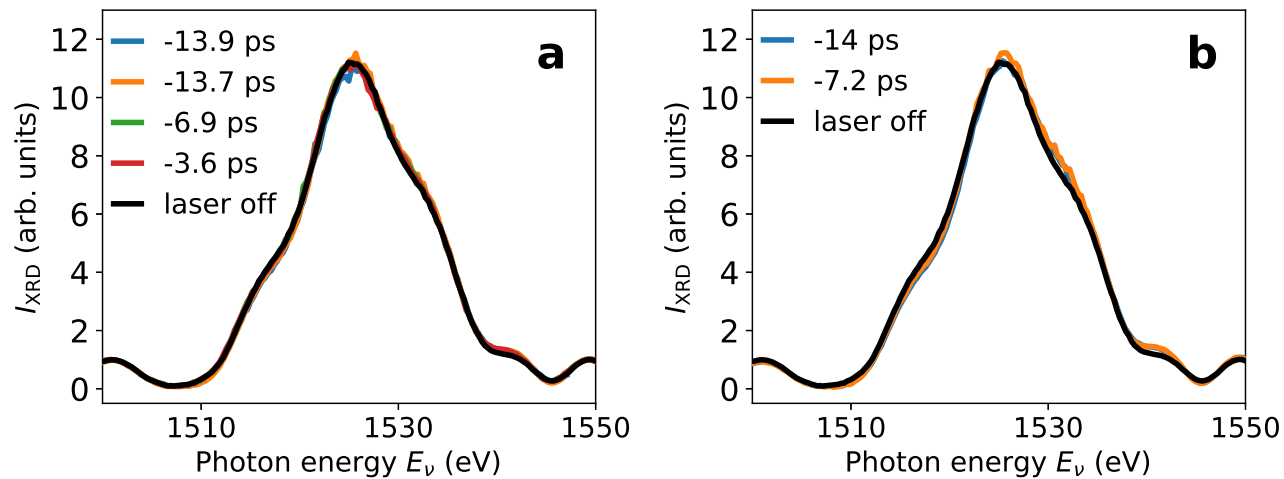


Figure S7. Comparison of $I_{\text{XRD}}(E_\nu)$ at negative delay and laser off. Comparison of laser off X-ray diffraction data $I_{\text{XRD}}(E_\nu)$ with data measured at negative delays, at incident fluence $F_{\text{in}} = 1.4 \text{ mJ cm}^{-2}$ (a) and $F_{\text{in}} = 2.7 \text{ mJ cm}^{-2}$ (b). The difference among different diffraction curves is negligible.

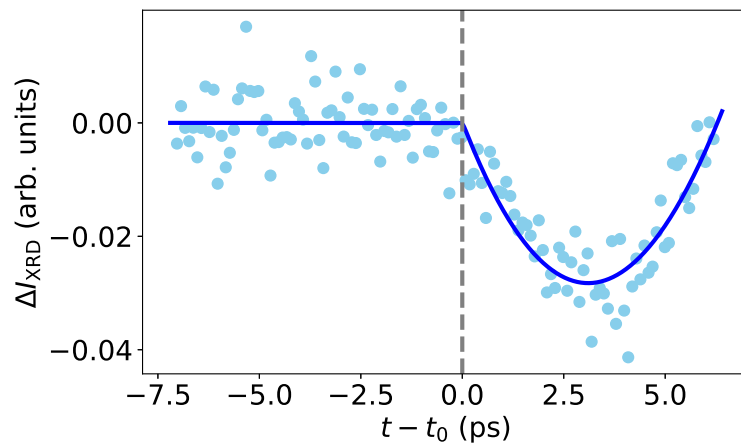


Figure S8. Determination of t_0 in tr-XRD experiments. The time delay t_0 corresponding to the temporal overlap of XFEL and OL during the tr-XRD measurements was determined by fitting high statistics $\Delta I_{\text{XRD}}(t - t_0)$ data at $E_v = 1525$ eV (shown here) using the fit function (S2) (Supplementary Note 2).

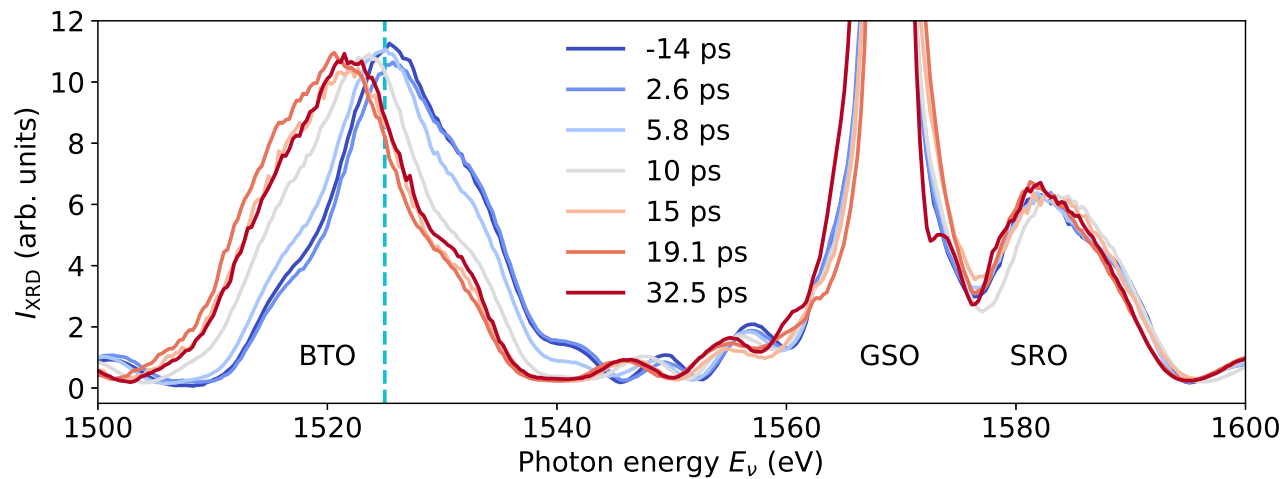


Figure S9. BTO, SRO and GSO (001) diffraction peaks. Time-resolved (001) Bragg peaks of the BTO/SRO/GSO sample at different time delays t . In contrast to the relatively large energy shifts of the BTO Bragg peak, the SRO and GSO (001) Bragg peaks show much weaker energy shifts, corresponding to changes of the average strain smaller than 0.05% and 0.02%, respectively.

Supplementary Note 4 Bunch arrival time monitor and time resolution of tr-XRD experiments

The bunch arrival time monitor (BAM) at the European XFEL tracks the arrival time of electron bunches in each pulse train, providing invaluable information to improve the time resolution of pump-probe experiments^{62,63}. The BAM measures the electron bunch arrival time with respect to the master clock that is also used to synchronize the pump laser. We employ the most downstream BAM, located at the end of the accelerator tunnel (1932 m from the laser gun) and about 1.5 km upstream of the interaction point at the sample position. In previous time-resolved experiments at the SCS Instrument, it has been observed that the time drifts measured by the BAM are amplified by 17% – 45% at the interaction point⁶⁴. In practice, this translates in a further correction of up to few tens of femtoseconds. In our experiments, the exact amplification coefficient is not known, thus we assume a direct proportionality between BAM and t_0 at the experiment, where t_0 indicates the temporal overlap between XFEL and optical laser. This assumption is justified by the dynamics of tr-XRD experiments taking place on the picosecond timescale (Figure 1).

We measure a standard deviation of the BAM within a pulse train of 10 fs, and a standard deviation of the BAM from train to train of 84 fs. Most importantly, slow drifts of the arrival time of FEL pulses over the course of hours are present and shown in Figure S10 for each recorded run. This indicates that without BAM correction, the time resolution of our experiments might be limited up to ≈ 600 fs, if we average non-consecutive runs. To improve our time resolution, the time delays of our data, indicating the relative time between FEL and optical laser pulses, are corrected for each pulse train according to the average BAM value of the respective pulse train. Thus, the resulting expected time resolution is $\Delta t = \sqrt{\tau_{\text{FEL}}^2 + \sigma_{\tau_{\text{FEL}}}^2 + \tau_{\text{OL}}^2 + \sigma_{\tau_{\text{OL}}}^2} \approx 90$ fs. This assumes an FEL pulse duration of $\tau_{\text{FEL}} \approx 35$ fs, including the nominal 25 fs pulse duration⁶⁵ and the pulse stretching at the monochromator of ≈ 10 fs (FWHM)⁶⁶, a pulse-to-pulse jitter in the train of $\sigma_{\tau_{\text{FEL}}} \approx 20$ fs, an optical laser pulse duration of $\tau_{\text{OL}} \approx 70$ fs and temporal jitter of $\sigma_{\tau_{\text{OL}}} \approx 30$ fs.

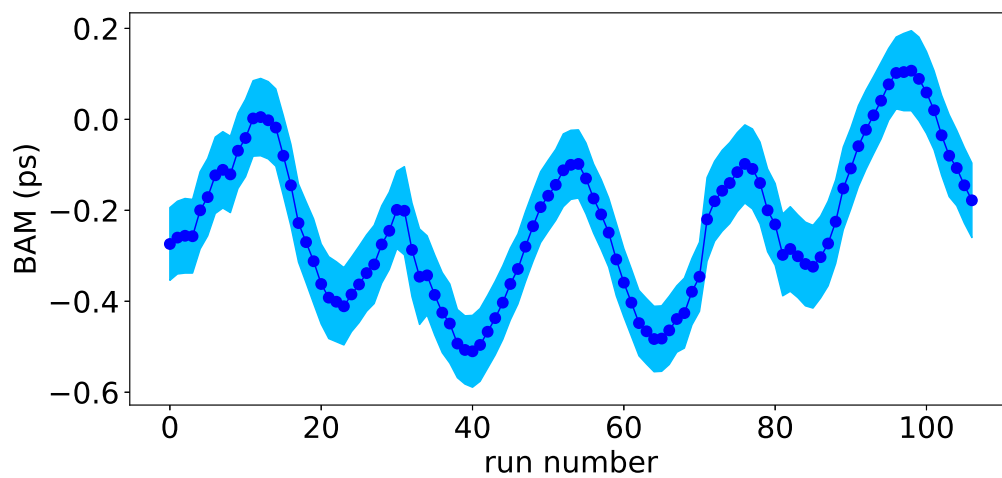


Figure S10. Beam arrival monitor. Mean (points) and standard deviation (shaded area) of the BAM values of consecutive runs (not evenly spaced in time) recorded within 60 h.

Supplementary Note 5 SHG and reflectivity data

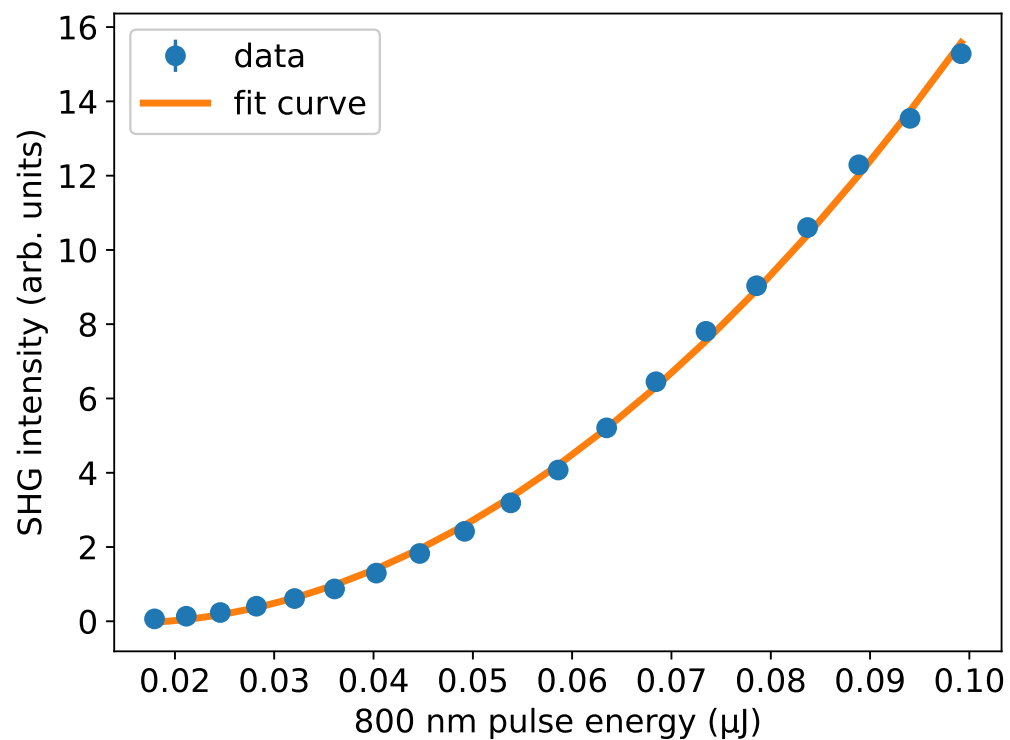


Figure S11. SHG intensity. SHG intensity measured as a function of the 800 nm probe pulse energy. The fit curve to the data is a polynomial of second order, thus it confirms the nonlinear nature of the signal measured by the photomultiplier.

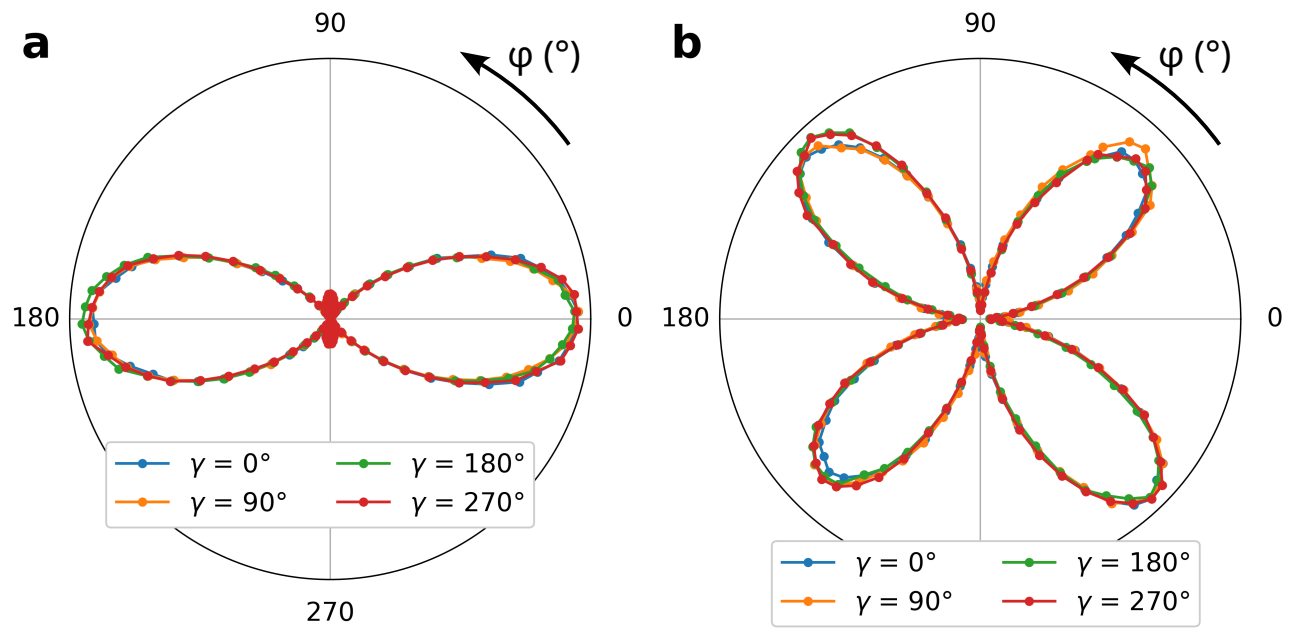


Figure S12. SHG plots at different azimuthal angles. Polar plots in *p*-out (a) and *s*-out (b) configuration measured at the four azimuthal angles $\gamma = 0^\circ, 90^\circ, 180^\circ, 270^\circ$. Regardless of the angle γ , the polar plots measured in the same polarization configuration overlap. This confirms the out-of-plane nature of the spontaneous polarization of our BTO sample. The presence of an in-plane component would manifest as different ϕ -dependence for different angles γ ⁶⁷.

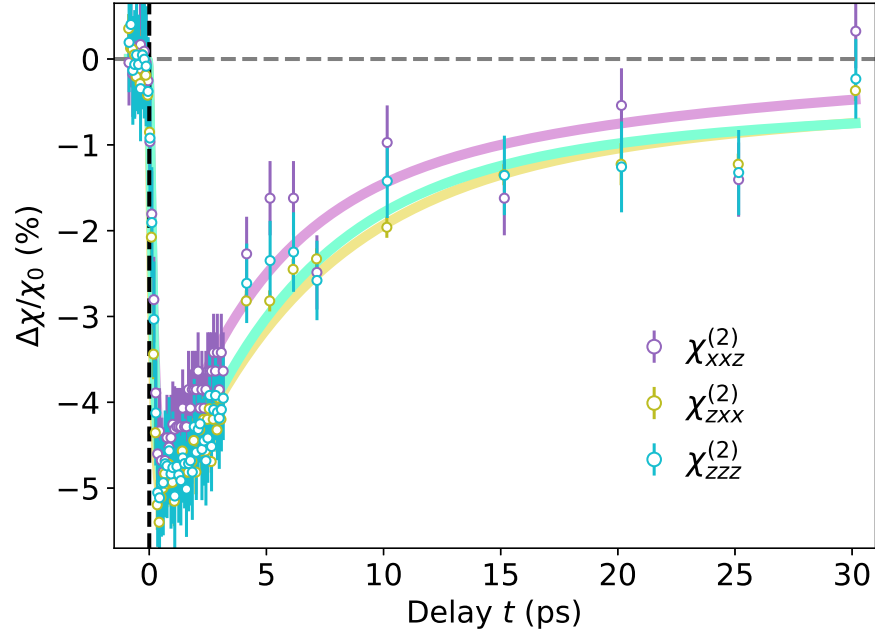


Figure S13. Delay dependence of the tensor elements $\chi_{xxz}^{(2)}$, $\chi_{zxx}^{(2)}$, and $\chi_{zzz}^{(2)}$. Relative change $\Delta\chi/\chi_0$ of the tensor elements $\chi_{xxz}^{(2)}$, $\chi_{zxx}^{(2)}$, and $\chi_{zzz}^{(2)}$ as a function of delay t , and corresponding fit curves given by equation (S2) (Supplementary Note 2). The fit results are: $\tau_0^{\chi_{xxz}} = 200(50)$ fs, $\tau_1^{\chi_{xxz}} = 4.2(22)$ ps, $\tau_2^{\chi_{xxz}} = 23.5(280)$ ps, $\tau_0^{\chi_{zxx}} = 160(30)$ fs, $\tau_1^{\chi_{zxx}} = 6.1(24)$ ps, $\tau_2^{\chi_{zxx}} = 49(119)$ ps, $\tau_0^{\chi_{zzz}} = 220(40)$ fs, $\tau_1^{\chi_{zzz}} = 5.6(22)$ ps, $\tau_2^{\chi_{zzz}} = 64(219)$ ps. The error bars refer to the standard deviation resulting from the fit of the tensor elements. The relatively small difference between $\chi_{zxx}^{(2)}$ (or $\chi_{zzz}^{(2)}$) and $\chi_{xxz}^{(2)}$ is due to the unfavorable experimental geometry with the polarization of the pump laser nearly perpendicular to P_s (Figure 2a), and it is expected to increase with the component of the pump polarization along P_s ³⁰.

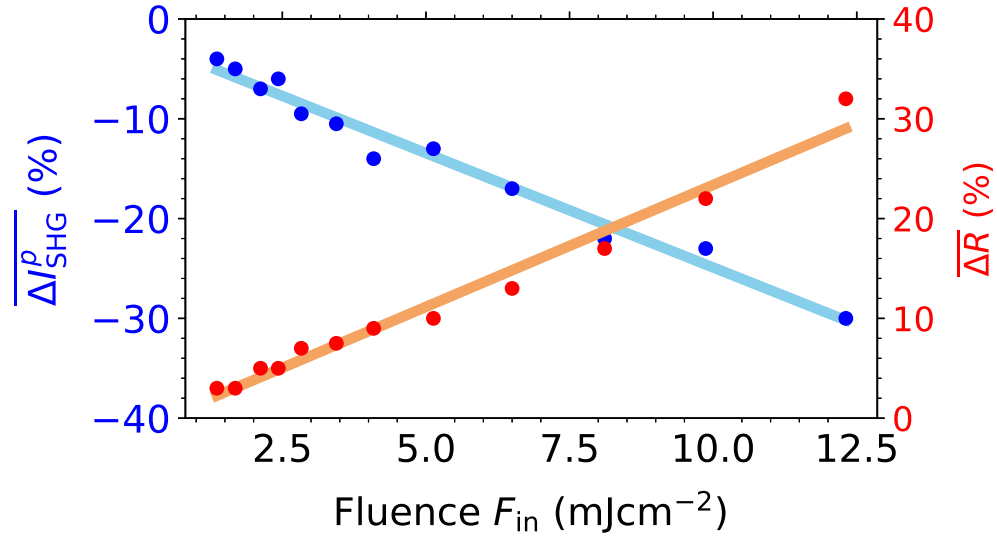


Figure S14. SHG and R maximum relative change. Maximum relative change of SHG ($\overline{\Delta I_{SHG}^p}$, blue points) and reflectivity ($\overline{\Delta R}$, red points) as a function of the incident pump fluence F_{in} . The parameters $\overline{\Delta I_{SHG}^p}$ and $\overline{\Delta R}$ are the average over the delay range $0.32 \text{ ps} < t < 0.73 \text{ ps}$ of $\Delta I_{SHG}^p / I_{SHG}^p$ and $\Delta R / R$, respectively (Figure S15). Blue and red lines are linear fits to the data. The error bars of each data point, equal to the standard deviation of $\Delta I_{SHG}^p / I_{SHG,0}^p$ and $\Delta R / R_0$ in the delay range $0.32 \text{ ps} < t < 0.73 \text{ ps}$, are not visible as they are approximately 1%.

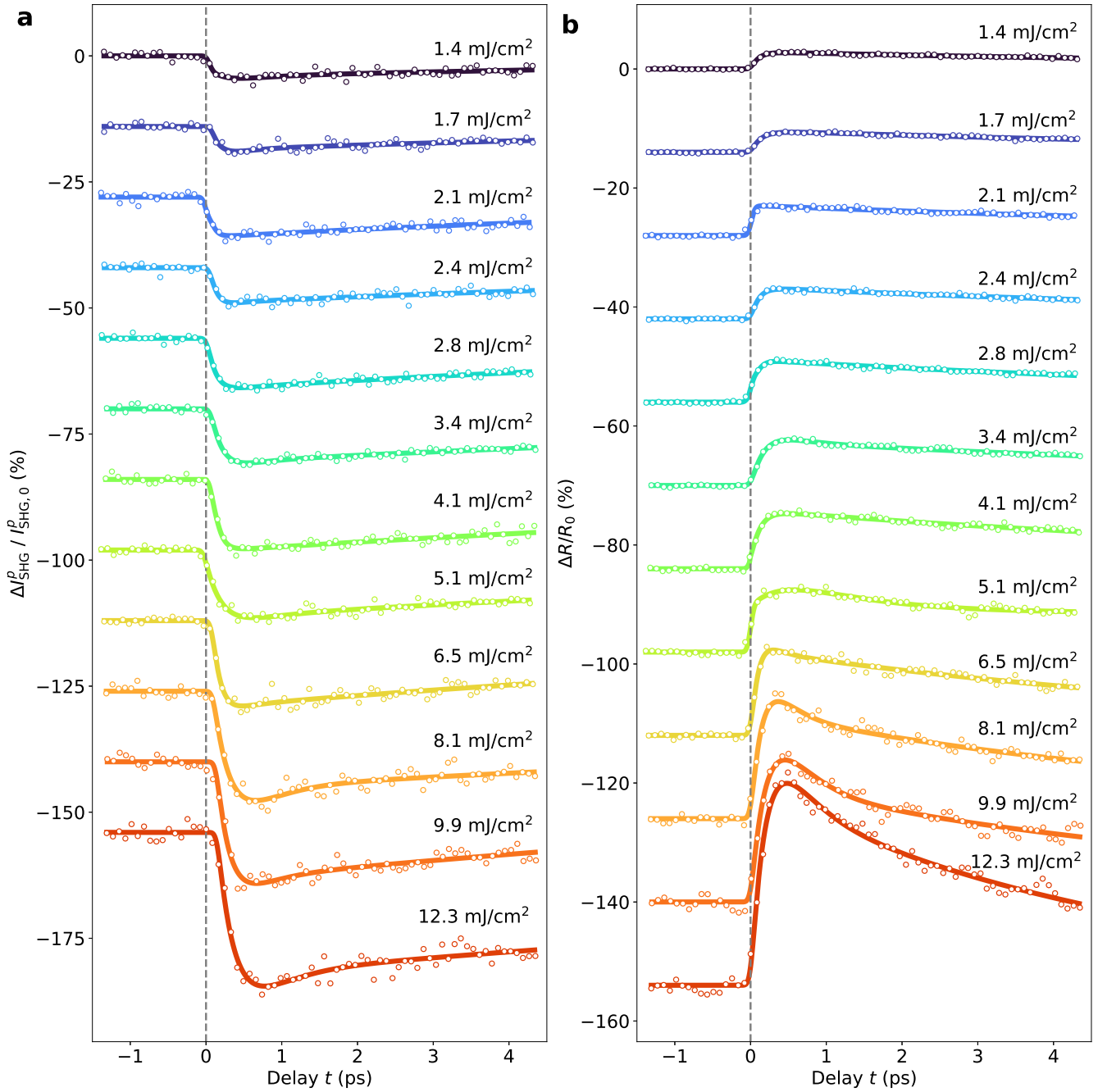


Figure S15. SHG and R time traces at different pump fluences. $\Delta I_{\text{SHG}}^p / I_{\text{SHG},0}^p$ (a) and $\Delta R / R_0$ (b) as a function of pump-probe delay t , measured at different incident pump laser fluences F_{in} marked on the figure. $\Delta I_{\text{SHG}}^p / I_{\text{SHG},0}^p$ data are measured at $\varphi = 0^\circ$. The maximum relative change of SHG ($\overline{\Delta I_{\text{SHG}}^p}$) and reflectivity ($\overline{\Delta R}$), shown in Figure S14 are derived from the data reported in this figure. Each time trace has an offset of -14% from the one above.

Supplementary Note 6 Sample properties

Supplementary Note 6.1 Transmittance profile of 266 nm beam in BTO/SRO/GSO

The transmittance of the 266 nm beam in our BTO/SRO/GSO sample, displayed in [Figure S16](#), is calculated as:

$$\begin{aligned}
 \mathcal{T}_{\text{BTO}}(z) &= \exp(-z/(\delta_{\text{BTO}} \cos \theta_t^{\text{BTO}})), \text{ for } 0 < z < d_{\text{BTO}} \\
 \mathcal{T}_{\text{SRO}}(z) &= \mathcal{T}_{\text{BTO}}(d_{\text{BTO}})(1 - R_p^{\text{SRO}}) \exp(-z/(\delta_{\text{SRO}} \cos \theta_t^{\text{SRO}})), \text{ for } d_{\text{BTO}} < z < d_{\text{BTO}} + d_{\text{SRO}} \\
 \mathcal{T}_{\text{GSO}}(z) &= \mathcal{T}_{\text{SRO}}(d_{\text{BTO}} + d_{\text{SRO}})(1 - R_p^{\text{GSO}}) \exp(-z/(\delta_{\text{GSO}} \cos \theta_t^{\text{GSO}})), \text{ for } z > d_{\text{BTO}} + d_{\text{SRO}}.
 \end{aligned}
 \tag{S3}$$

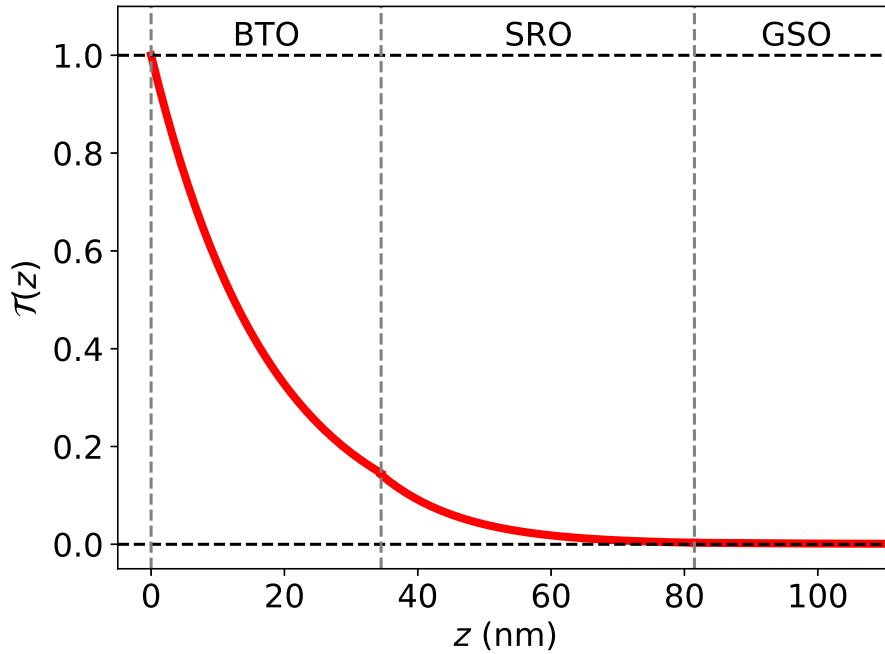


Figure S16. Transmittance profile. Transmittance profile $\mathcal{T}(z)$ of the 266 nm pump laser in our BTO/SRO/GSO sample employing penetration depths δ and reflectivities R_p reported in [Table S2](#). The dashed gray lines mark the BTO surface, the BTO/SRO and the SRO/GSO interfaces.

The penetration depths δ_{BTO} , δ_{SRO} and δ_{GSO} are calculated as detailed in [Supplementary Note 6.2](#). The reflections at the air-BTO, BTO-SRO, and SRO-GSO interfaces ([Table S2](#)) are determined by using Snell's law $n_1 \sin \theta_i = n_2 \sin \theta_t$ and the Fresnel equation for p -polarized light $R_p = |(n_1 \cos \theta_i - n_2 \cos \theta_t)/(n_1 \cos \theta_i + n_2 \cos \theta_t)|^2$. Here, n_1 and n_2 are the real part of n^* at the two sides of the interface, while θ_i and θ_t are the angles of the incident and the transmitted beam with respect to the surface normal, with $\theta_i^{\text{BTO}} = 4^\circ$. The index of refraction of SRO and GSO are calculated from Ref.⁶⁸, as detailed in [Supplementary Note 6.2](#), while the index of refraction of the BTO thin film is determined from ellipsometry data at 266 nm in Ref.²⁸.

Given the parameters above (summarized in [Table S2](#)), the absorbed fluences in the BTO and SRO thin films are calculated

as:

$$F_{\text{abs}}^{\text{BTO}} = F_{\text{in}}(1 - R_p^{\text{BTO}})(1 - \exp(-d_{\text{BTO}}/(\delta_{\text{BTO}} \cos \theta_i^{\text{BTO}}))) = 0.7F_{\text{in}} \quad (\text{S4})$$

$$F_{\text{abs}}^{\text{SRO}} = F_{\text{in}}(1 - R_p^{\text{BTO}}) \exp[-d_{\text{BTO}}/(\delta_{\text{BTO}} \cos \theta_i^{\text{BTO}})](1 - R_p^{\text{SRO}})[1 - \exp(-d_{\text{SRO}}/(\delta_{\text{SRO}} \cos \theta_i^{\text{SRO}}))] = 0.12F_{\text{in}}, \quad (\text{S5})$$

and are reported in [Table S1](#).

Table S1. Absorbed fluences in BTO and SRO thin films. Absorbed fluences in BTO and SRO thin films at two different incident fluences F_{in} .

F_{in} (mJ cm^{-2})	$F_{\text{abs}}^{\text{BTO}}$ (mJ cm^{-2})	$F_{\text{abs}}^{\text{SRO}}$ (mJ cm^{-2})
1.4	0.98	0.17
2.7	1.88	0.33

Supplementary Note 6.2 Penetration depths

The absorption coefficient α of the 266 nm pump laser in our BTO thin film is determined based on the study of α as a function of strain in Ref.²⁸. For a compressive strain of -0.55% , the penetration depth is $\delta_{\text{BTO}} = 1/\alpha_{\text{BTO}} = 17.9$ nm. The penetration depths in the SRO thin film $\delta_{\text{SRO}} = 21.5$ nm and in the GSO substrate $\delta_{\text{GSO}} = 26.1$ nm are determined from the respective dielectric constants ϵ_1 and ϵ_2 , reported in Ref.⁶⁸. Specifically, $\delta = 1/\alpha = \lambda/(4\pi k)$, where $\lambda = 266$ nm is the wavelength of the pump laser, and k is the imaginary part of the complex index of refraction $n^* = n + ik$, with $n = \sqrt{(|\epsilon^*| + \epsilon_1)/2}$, $k = \sqrt{(|\epsilon^*| - \epsilon_1)/2}$, and $|\epsilon^*| = \sqrt{\epsilon_1^2 + \epsilon_2^2}$. The penetration depth of 800 nm and 400 nm in BTO, $\delta_{\text{BTO}}^{800\text{nm}} = 944$ nm and $\delta_{\text{BTO}}^{400\text{nm}} = 167$ nm, are obtained from the equations above, calculating the complex dielectric function as $\epsilon^* = \epsilon_1 + i\epsilon_2 = \sin \theta_i^2 [1 + \tan \theta_i^2 (\frac{1-\rho}{1+\rho})^2]$, where $\rho = \tan \Psi \exp(i\Delta)$, with Ψ and Δ reported in Ref.²⁸. Due to the large penetration depths $\delta_{\text{BTO}}^{800\text{nm}}$ and $\delta_{\text{BTO}}^{400\text{nm}}$, we probe the entire BTO thickness ($d_{\text{BTO}} = 34.5$ nm).

Table S2. Physical constants used in the calculation of two-temperature model and strain model. The film thicknesses d result from θ - 2θ measurements (Figure S1). The penetration depth δ and the reflectivity R_p are discussed in Supplementary Note 6.1 and Supplementary Note 6.2. The volumetric heat capacities C_e and C_p of SRO and GSO are calculated from Refs.⁶⁹ and⁷⁰, respectively, while those of BTO are discussed in Supplementary Note 7. The mass density ρ , the bulk modulus B , and the Poisson ratio ν are taken from Ref.⁷¹. The longitudinal sound velocity $v = \sqrt{3B(1-\nu)/[\rho(1+\nu)]}$ ⁴¹. The linear expansion coefficient β of SRO and GSO, and $\beta_{T>T_c}$ of BTO are obtained from data shown in Figure S4, while $\bar{\beta}_{T<T_c}$ of BTO is a fit parameter, as discussed in Supplementary Note 8. The thermal conductivity K_p and diffusivity $D_p = K_p/C_p$ are given in the respective references reported in the Table below. The acoustic reflection coefficient is given by $R_Z = (Z_2 - Z_1)/(Z_2 + Z_1)$, where Z_1 and Z_2 are the acoustic impedances at the two sides of the interface, with $Z = \rho v$ and the strain wave travelling from material 1 to 2. For example, going from BTO to SRO, $R_Z = 0.13$, while going from BTO to the vacuum interface, $R_Z = -1$.

constants	unit	BTO	SRO	GSO
d	nm	34.5	47	0.5×10^6
δ	nm	17.9	21.5	26.1
R_p	-	0.178	0.022	0.018
C_p	$\text{J m}^{-3} \text{K}^{-1}$	2.8×10^6	2.8×10^{669}	2.1×10^{670}
C_e	$\text{J m}^{-3} \text{K}^{-1}$	4.2×10^4	2.3×10^{569}	9×10^{470}
ρ ⁷¹	g cm^{-3}	5.93	6.46	6.6
m ⁷²	g mol^{-1}	233.19	236.69	250.2
β	K^{-1}	1.33×10^{-5} ($\beta_{T>T_c}$)	1.58×10^{-5}	0.76×10^{-5}
K_p	$\text{W m}^{-1} \text{K}^{-1}$	2.73 ⁷³	5.72 ⁶⁹	2.53 ⁷⁰
D_p	$\text{mm}^2 \text{s}^{-1}$	1.11 ⁷³	2.05 ⁶⁹	1.22 ⁷⁰
B ⁷¹	GPa	107	166	163
ν ⁷¹	-	0.3	0.31	0.29
v ⁴¹	m s^{-1}	5399	6372	6386
Z	$\text{kg m}^{-2} \text{s}^{-1}$	3.2×10^7	4.1×10^7	4.2×10^7
R_Z	-	-1	0.13	0.01

Supplementary Note 7 Two-temperature model

Electron and phonon temperatures, $T_e(z, t)$ and $T_p(z, t)$, result from the analytical solution of the two-temperature model (2TM), consisting of the following coupled equations⁷⁴:

$$\begin{aligned} C_e \frac{\partial T_e}{\partial t} &= -g(T_e - T_p) + S(z, t), \\ C_p \frac{\partial T_p}{\partial t} &= g(T_e - T_p), \end{aligned} \quad (\text{S6})$$

where C_e and C_p are volumetric heat capacities, respectively, and g is the electron-phonon coupling. The source term $S(z, t)$ represents the absorbed power density (W m^{-3}) of the pump laser in our sample as a function of t and z . It is defined as $S(z, t) = F_{\text{abs}} \exp(-z/(\delta \cos \theta_t)) \exp(-t^2/(2\tau_{\text{OL}}^2))/(\delta \tau_{\text{OL}})$, where F_{abs} is the pump absorbed fluence (Supplementary Note 6.1), δ is the penetration depth (Supplementary Note 6.2), θ_t is the angle of the transmitted optical beam with respect to the surface normal, and τ_{OL} is the optical laser pulse duration (Supplementary Note 4).

In general, equation (S6) contains also the diffusion terms $K_e \partial^2 T_e / \partial z^2$ and $K_p \partial^2 T_p / \partial z^2$, where K_e and K_p are carrier and thermal conductivity, respectively. In the particular case of BTO, carrier and thermal diffusion terms can be neglected because the parameters $D_e / (v \delta_{\text{BTO}}) = 2.5 \times 10^{-5}$ and $D_p / (v \delta_{\text{BTO}}) = 1.1 \times 10^{-2}$ are relatively small. Here, the electron diffusion coefficient is calculated from the Einstein relation $D_e = \mu k_B T / q = 2.6 \times 10^{-7} \text{ m}^2 \text{ s}^{-1}$, where $\mu = 0.1 \text{ cm}^2 \text{ V}^{-1} \text{ s}^{-1}$ is the BTO electron mobility⁷⁵, k_B is the Boltzmann constant, T is the sample temperature and q is the electron charge, while the BTO thermal diffusivity⁷³ is $D_p = 1.11 \text{ mm}^2 \text{ s}^{-1}$.

We turn now to discuss the volumetric heat capacities C_e and C_p . Electron and phonon volumetric heat capacities of SRO and GSO are taken from Refs.^{69,70}, assuming $T = 300 \text{ K}$. This assumption is justified by the fact that in GSO the transmittance of the 266 nm beam is essentially 0%, while in the SRO thin film only 12% of the incident fluence is absorbed. For the absorbed fluence $F_{\text{abs}} = 0.33 \text{ mJ cm}^{-2}$ (Supplementary Note 6.1), the maximum temperature increase⁴¹ in SRO is $\Delta T = F_{\text{abs}}^{\text{SRO}} / (\delta_{\text{SRO}} C_p^{\text{SRO}}) = 55 \text{ K}$, with a consequent increase of C_p^{SRO} of only 2%. Conversely, C_e^{SRO} increases by 18%, but the absolute value remains one order of magnitude smaller than C_p^{SRO} . The volumetric heat capacity C_p^{BTO} as a function of T is reported in Ref.⁷⁶. Given the weak temperature dependence for $T > 300 \text{ K}$, we consider $C_p^{\text{BTO}} = 2.8 \times 10^6 \text{ J m}^{-3} \text{ K}^{-1}$ and calculate $\Delta T = F_{\text{abs}}^{\text{BTO}} / (\delta_{\text{BTO}} C_p^{\text{BTO}}) = 375 \text{ K}$ and 196 K , for $F_{\text{abs}}^{\text{BTO}} = 1.88 \text{ mJ cm}^{-2}$ and 0.98 mJ cm^{-2} (Supplementary Note 6.1), respectively. Due to the weak dependence on T , the average of C_p^{BTO} between 300 K and $300 \text{ K} + \Delta T$ yields the self-consistent result of $C_p^{\text{BTO}} = 2.8 \times 10^6 \text{ J m}^{-3} \text{ K}^{-1}$ ⁷⁶. Finally, to estimate C_e^{BTO} , we rely on the available data from other titanates, e.g. SrTiO_3 ⁷⁷ and CaTiO_3 ⁷⁸, and observe that they have an average ratio $C_e / C_p = 0.015$ for the T ranges considered here. This yields $C_e^{\text{BTO}} = 4.2 \times 10^4 \text{ J m}^{-3} \text{ K}^{-1}$. Although C_e^{BTO} is a temperature-dependent quantity, for simplicity, we assume it to be constant here. For completeness, all the physical constants employed in the solution of the 2TM are reported in Table S2.

We focus now on the analytical solution of the 2TM. The second equation of equation (S6) can be written as:

$$T_e = \frac{C_p}{g} \frac{\partial T_p}{\partial t} + T_p, \quad (\text{S7})$$

which is then inserted in the first equation of (S6) and yields the following second order differential equation of T_p :

$$\frac{C_e C_p}{g} \frac{\partial^2 T_p}{\partial t^2} + (C_e + C_p) \frac{\partial T_p}{\partial t} = S(z, t). \quad (\text{S8})$$

Given the following initial and boundary conditions: $T_e(z, 0) = T_p(z, 0) = T_0 = 300 \text{ K}$, $\partial T_p / \partial z(0, t) = 0$, $\partial T_p / \partial t(z, 0) = 0$, we can derive the lattice temperature $T_p(z, t)$ as an analytical solution of equation (S8):

$$\begin{aligned} T_p(z, t) = T_0 + \frac{\sqrt{\pi} \mathcal{L} \tau_{\text{OL}}}{\sqrt{2} \mathcal{B}} \exp\left(\frac{\tau_{\text{OL}}^2 \mathcal{B}^2}{2 \mathcal{A}^2}\right) \text{erf}\left(\frac{\mathcal{B} \tau_{\text{OL}}}{\sqrt{2} \mathcal{A}} - \frac{t}{\sqrt{2} \tau_{\text{OL}}}\right) \exp\left(-\frac{z}{\delta}\right) \exp\left(-\frac{\mathcal{B}}{\mathcal{A}} t\right) \\ + \frac{\sqrt{\pi} \mathcal{L} \tau_{\text{OL}}}{\sqrt{2} \mathcal{B}} \exp\left(-\frac{z}{\delta}\right) \text{erf}\left(\frac{1}{\sqrt{2} \tau_{\text{OL}}} t\right) \\ - \frac{\sqrt{\pi} \mathcal{L} \tau_{\text{OL}}}{\sqrt{2} \mathcal{B}} \exp\left(\frac{\tau_{\text{OL}}^2 \mathcal{B}^2}{2 \mathcal{A}^2}\right) \text{erf}\left(\frac{\mathcal{B} \tau_{\text{OL}}}{\sqrt{2} \mathcal{A}}\right) \exp\left(-\frac{z}{\delta}\right) \exp\left(-\frac{\mathcal{B}}{\mathcal{A}} t\right), \end{aligned} \quad (\text{S9})$$

where $\mathcal{A} = C_e C_p / g$, $\mathcal{B} = C_e + C_p$, and $\mathcal{L} = (1/\delta) F_{\text{abs}}$. Substituting equation (S9) in equation (S7) we obtain the electron temperature $T_e(z, t)$:

$$\begin{aligned} T_e(z, t) = T_0 - \frac{\sqrt{\pi} \mathcal{L} \tau_{\text{OL}}}{\sqrt{2} \mathcal{B}} \frac{C_p}{C_e} \exp\left(\frac{\tau_{\text{OL}}^2 \mathcal{B}^2}{2 \mathcal{A}^2}\right) \text{erf}\left(\frac{\mathcal{B} \tau_{\text{OL}}}{\sqrt{2} \mathcal{A}} - \frac{t}{\sqrt{2} \tau_{\text{OL}}}\right) \exp\left(-\frac{z}{\delta}\right) \exp\left(-\frac{\mathcal{B}}{\mathcal{A}} t\right) \\ + \frac{\sqrt{\pi} \mathcal{L} \tau_{\text{OL}}}{\sqrt{2} \mathcal{B}} \exp\left(-\frac{z}{\delta}\right) \text{erf}\left(\frac{1}{\sqrt{2} \tau_{\text{OL}}} t\right) \\ + \frac{\sqrt{\pi} \mathcal{L} \tau_{\text{OL}}}{\sqrt{2} \mathcal{B}} \frac{C_p}{C_e} \exp\left(\frac{\tau_{\text{OL}}^2 \mathcal{B}^2}{2 \mathcal{A}^2}\right) \text{erf}\left(\frac{\mathcal{B} \tau_{\text{OL}}}{\sqrt{2} \mathcal{A}}\right) \exp\left(-\frac{z}{\delta}\right) \exp\left(-\frac{\mathcal{B}}{\mathcal{A}} t\right). \end{aligned} \quad (\text{S10})$$

The dependence of T_e and T_p (averaged over d_{BTO}) on the delay t is reported in Figure S17 for the two incident pump fluences $F_{\text{in}} = 1.4 \text{ mJ cm}^{-2}$ and 2.7 mJ cm^{-2} and the corresponding fit parameter g (Table S3), while Figure S22a and Figure S21a report the 2D maps of $T_p(z, t)$ as a function of delay t and depth z at the respective fluences.

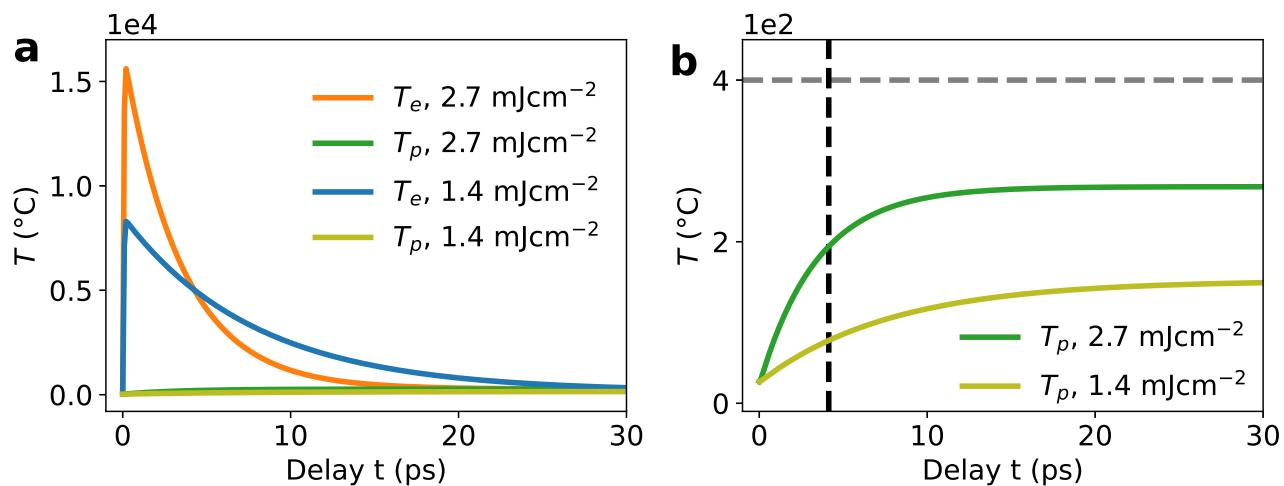


Figure S17. Electron and lattice temperature as a function of delay t . (a) T_e and T_p averaged over d_{BTO} as a function of delay t for the incident pump fluences $F_{\text{in}} = 1.4 \text{ mJcm}^{-2}$ and $F_{\text{in}} = 2.7 \text{ mJcm}^{-2}$, calculated as detailed in [Supplementary Note 7](#). (b) the same as panel (a) with focus on the temperature range of T_p . The gray dashed line indicates $T_c = 400^{\circ}\text{C}$ ([Figure S4](#)).

Supplementary Note 8 Strain model

The total stress experienced by our sample upon optical laser excitation can be written as^{4,32}:

$$\sigma = \rho v^2 \eta + \sigma_{DP} \left(T_e, \frac{\partial E_g}{\partial p} \right) + \sigma_{TE}(T_p, \beta), \quad (\text{S11})$$

where $Y = \rho v^2$ is the Young's modulus, ρ is the mass density and v is the longitudinal speed of sound (Table S2). The first term in equation (S11) indicates the direct relationship between the stress σ , a force that induces a deformation of the material, and the strain η that represents the resulting deformation of the material. The stress σ causes the generation of a strain wave that propagates through the material and across the interface to the layer below. In equation (S11), $\partial E_g / \partial p$ indicates the variation of the bandgap as a function of the electronic pressure, and β is the linear expansion coefficient.

Equation (S11) can be written more explicitly as³²:

$$\sigma(z, t) = \rho v^2 \eta(z, t) - n_e B \frac{\partial E_g}{\partial p} - 3B\beta(T_p(z, t) - T_0), \quad (\text{S12})$$

where $n_e = C_e(T_e(z, t) - T_0)/(E - E_g)$ is the carrier density⁴ (with unit m^{-3}), B is the bulk modulus (Table S2), $T_0 = 300\text{K}$ is the sample temperature at equilibrium, and $n_e(E - E_g)$ is the total energy density transferred from the optical photons to the electronic subsystem⁴. We consider here only the dependence of T_e , T_p and η on the z direction (sample depth). This one-dimensional approximation is justified by the large ratio between the laser excited area and the BTO thickness, leading to the film contraction/expansion only along the surface normal on the few tens of picoseconds timescale.

The relation between the stress σ and the atomic displacement u is described by the following one-dimensional lattice strain wave equation⁴¹:

$$\rho \frac{\partial^2 u(z, t)}{\partial t^2} = \frac{\partial \sigma(z, t)}{\partial z}, \quad (\text{S13})$$

which can be recast as a function of $\eta(z, t) = \partial u(z, t) / \partial z$:

$$\frac{\partial^2 \eta(z, t)}{\partial t^2} = \frac{1}{\rho} \frac{\partial^2 \sigma(z, t)}{\partial z^2}. \quad (\text{S14})$$

Substituting equation (S12) in equation (S14) yields:

$$\frac{\partial^2 \eta(z, t)}{\partial t^2} = v^2 \frac{\partial^2 \eta(z, t)}{\partial z^2} - \frac{C_e}{\rho(E - E_g)\delta^2} B \frac{\partial E_g}{\partial p} (T_e(z, t) - T_0) - \frac{3B\beta}{\rho\delta^2} (T_p(z, t) - T_0). \quad (\text{S15})$$

Given the initial conditions⁴¹ $\eta(z, 0) = 0$, $\partial \eta / \partial t(z, 0) = 0$, $\sigma(0, t) = 0$, equation (S15) provides the out-of-plane strain profile

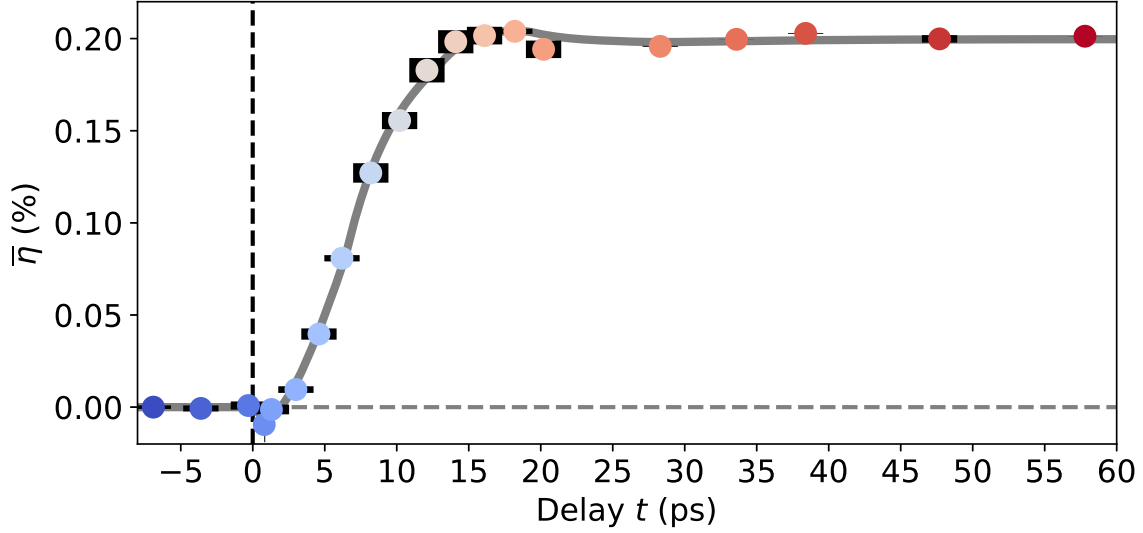


Figure S18. $\bar{\eta}(t)$ with pump fluence $F_{\text{in}} = 1.4 \text{ mJ cm}^{-2}$. Average BTO out-of-plane strain $\bar{\eta}(t)$ as a function of pump-probe delay t , measured with the incident pump fluence $F_{\text{in}} = 1.4 \text{ mJ cm}^{-2}$. The error bars follow from the determination of c from $I_{\text{XRD}}(E_V) \pm \text{SD}$, where SD is the standard deviation. The solid gray line is a fit to the data.

$\eta(z, t)$ by solving the following analytical integrals⁷⁹:

$$\eta(z, t) = \begin{cases} \frac{1}{2v} \int_0^t \int_{z-v(t-\tau)}^{z+v(t-\tau)} \mathfrak{F}(\xi, \tau) d\xi d\tau, & \text{for } t < \frac{z}{v} \\ \frac{1}{2v} \int_0^{t-\frac{z}{v}} \int_{v(t-\tau)-z}^{z+v(t-\tau)} \mathfrak{F}(\xi, \tau) d\xi d\tau \\ + \frac{1}{2v} \int_{t-\frac{z}{v}}^t \int_{z-v(t-\tau)}^{z+v(t-\tau)} \mathfrak{F}(\xi, \tau) d\xi d\tau + \mathfrak{F}(0, t-z/v) \frac{\delta^2}{v^2}, & \text{for } t > \frac{z}{v}, \end{cases} \quad (\text{S16})$$

where $\mathfrak{F}(z, t) = -C_e B \frac{\partial E_g}{\partial p} (T_e(z, t) - T_0) / [\rho(E - E_g) \delta^2] - 3B\beta (T_p(z, t) - T_0) / (\rho \delta^2)$. Electron and phonon temperatures, $T_e(z, t)$ and $T_p(z, t)$, are determined using the 2TM (Supplementary Note 7).

Since the optical pump laser is absorbed mostly in the BTO thin film, but partially also in the SRO layer, there will be two strain waves originating at the vacuum/BTO and the BTO/SRO interfaces. These strain waves propagate through the sample and reflect at each interface, with acoustic reflection coefficients R_Z (Table S2). The almost identical acoustic impedance of SRO and GSO, leads to a $R_Z = 1\%$ at the SRO/GSO interface. Conversely, the strain wave undergoes a 13% reflection at the BTO/SRO interface and 100% reflection at the interface with vacuum, given the acoustic impedance $Z_{\text{vacuum}} = 0$ (Table S2). The superposition of the generated and reflected strain waves yields a total strain wave $\eta(z, t)$, which is then averaged over the BTO film thickness to obtain $\bar{\eta}(t) = \int_0^{d_{\text{BTO}}} \eta(z, t) dz / d_{\text{BTO}}$. This quantity is used to fit the experimental average strain data obtained from tr-XRD measurements for $F_{\text{in}} = 2.7 \text{ mJ cm}^{-2}$ (Figure 1d) and for $F_{\text{in}} = 1.4 \text{ mJ cm}^{-2}$ (Figure S18), with the resulting fit parameters ($\partial E_g / \partial p$, $\bar{\beta}_{T < T_c}$, and g) reported in Table S3. The parameter $\partial E_g / \partial p$ has been discussed in the main text, we focus here on the discussion of $\bar{\beta}_{T < T_c}$, and g fit results, while the calculations based on our strain model are presented in Supplementary Note 8.

Table S3. Strain model fit results. Fit results of the experimental $\bar{\eta}(t)$ curves in Figure 1d and Figure S18, including $\partial E_g/\partial p$, the linear expansion coefficient $\bar{\beta}_{T < T_c}$ and the electron-phonon coupling g , measured at two different incident pump fluences F_{in} .

F_{in} (mJcm ⁻²)	$\partial E_g/\partial p$ (JPa ⁻¹)	$\bar{\beta}_{T < T_c}$ (K ⁻¹)	g (Wm ⁻³ K ⁻¹)
1.4	$-3.0(4) \times 10^{-31}$	$8.5(1) \times 10^{-6}$	$6.5(2) \times 10^{15}$
2.7	$-3.0(5) \times 10^{-31}$	$2.5(2) \times 10^{-6}$	$1.2(1) \times 10^{16}$

The linear expansion coefficient $\bar{\beta}_{T < T_c}$ is the fit parameter referring to the average β in the range $T_0 < T < T_c$, with Curie temperature $T_c = 400^\circ\text{C}$. While for $T > T_c$, the linear expansion coefficient β is constant and positive ($\beta_{T > T_c} = 1.33 \times 10^{-5} \text{K}^{-1}$), it is positive for $T_0 < T < T^*$, and negative for $T^* < T < T_c$ (Figure S4). In our sample, the temperature below T_c at which β changes sign is $T^* = 200^\circ\text{C}$ (Figure S4). Based on our model, in the metastable state ($t > 20$ ps), only ≈ 7 nm of the BTO film is at $T^* < T < T_c$ for $F_{in} = 1.4 \text{mJcm}^{-2}$, while ≈ 14 nm of the BTO film is at $T^* < T < T_c$ for $F_{in} = 2.7 \text{mJcm}^{-2}$ (Figure S19). As a result, in the latter case the portion of the sample at $\beta < 0$ is larger than in the former case, thus $\bar{\beta}_{T < T_c}$ is expected to be smaller, as shown by our fit results (Table S3). At the same time, for both fluences, the larger portion of the sample ($\approx 14 - 27$ nm) is at $T_0 < T < T^*$, hence $\bar{\beta}_{T < T_c}$ is expected to be positive, as obtained by our fit results.

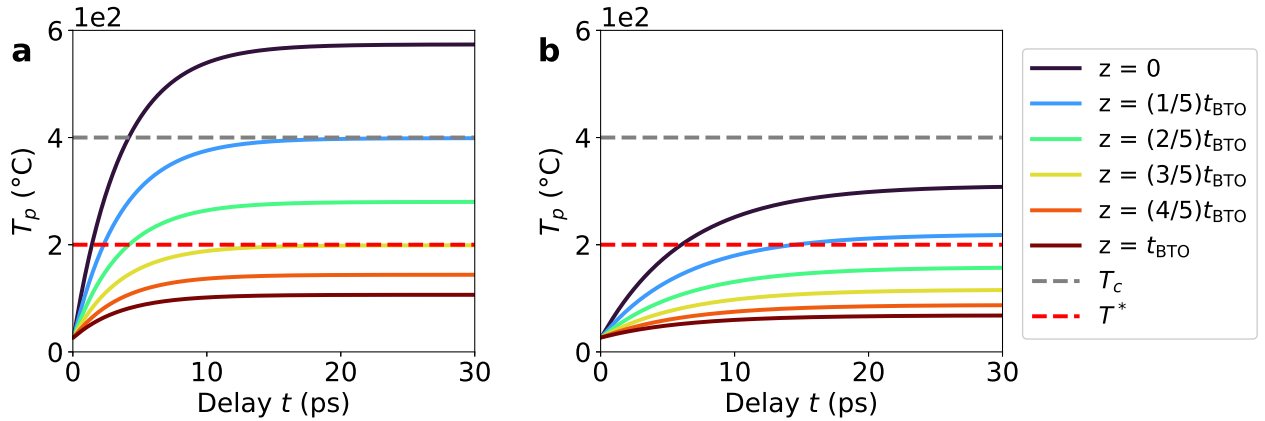


Figure S19. Lattice temperature as a function of delay and depth. T_p at different depths z from the surface ($z = 0$) as a function of delay t for $F_{in} = 2.7 \text{mJcm}^{-2}$ (a) and $F_{in} = 1.4 \text{mJcm}^{-2}$ (b). The dashed gray[red] line indicates T_c [T^*].

The electron-phonon coupling g of the 2TM (Supplementary Note 7) is a temperature dependent quantity, however for simplicity in our model it is assumed to be constant, similarly to most current investigations of short-pulse laser excitation⁸⁰. In general, the dependence of g on T_e is related to the electron density of states, and, if the d band electrons are below the Fermi level without crossing it (as in BTO), g increases with T_e . In particular, within the free electron gas model⁸⁰, g is linearly dependent on the electron density n_e . This approximation is expected to be valid for relatively low electron temperatures⁸¹, as in our case. In fact, the resulting g fit parameters (Table S3) scale approximately as the peak electron density given by $n_{e,max} = C_e(T_{e,max} - T_0)/(E - E_g)^4$ (Figure S20). Specifically, $n_{e,max} = 1.7 \times 10^{27} \text{m}^{-3}$ and $3.2 \times 10^{27} \text{m}^{-3}$

for $F_{in} = 1.4 \text{ mJcm}^{-2}$ and 2.7 mJcm^{-2} , respectively. For comparison, the electron density in copper, with one electron per atom in the conduction band ($N_e = 1$), is $n_e^{Cu} = N_e \rho N_A / M = 8.5 \times 10^{28} \text{ m}^{-3}$, where $\rho = 8.96 \text{ gcm}^{-3}$ is the mass density⁸², $N_A = 6.022 \times 10^{23} \text{ atoms/mol}$ is the Avogadro's number⁸³, and $M = 63.55 \text{ g mol}^{-1}$ is the atomic mass⁸². The absolute value of the fit g parameters are of similar order of magnitude as for SrRuO_3 ³⁷ and other perovskites⁸⁴. Moreover, it is worth noting that the obtained electron densities and the fit g values are more than one order of magnitude smaller than the corresponding parameters in metals^{80,85,86}, e.g., the electron-phonon coupling in Cu ⁸⁰ is $g \approx 5 \times 10^{17} \text{ W m}^{-3} \text{ K}^{-1}$.

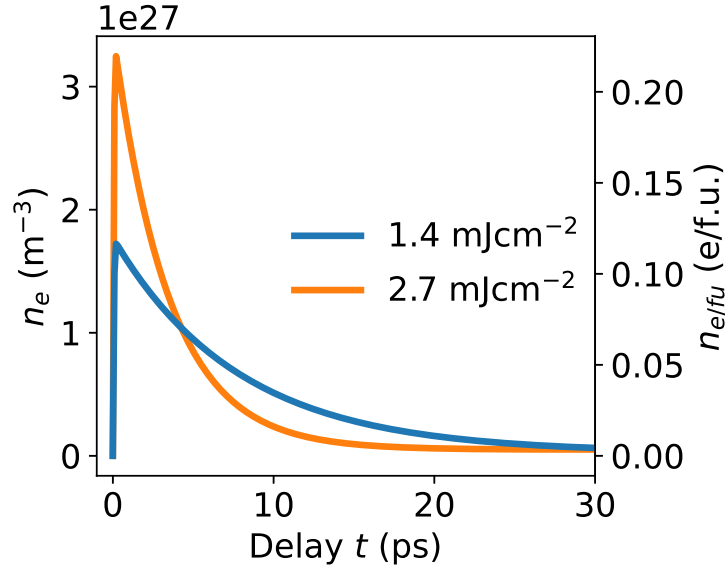


Figure S20. Electron density as a function of delay. Electron density calculated as $n_e = C_e(T_e(t) - T_0)/(E - E_g)^4$ for two different pump fluences, and corresponding concentration of photoexcited electrons per formula unit (e/f.u.) $n_{e/fu}$, where $n_{e/fu} = n_e V$ with the formula unit volume $V = c_0^3 = 67.62 \times 10^{-30} \text{ m}^3$. Here, $T_e(t)$ refers to the electron temperature averaged over d_{BTO} .

Supplementary Note 9 Temperature, strain and diffraction curve calculations

Given the fit parameters in [Table S3](#), we calculate the lattice temperature $T_p(z,t)$ in the BTO thin film for $F_{\text{in}} = 2.7 \text{ mJcm}^{-2}$ ([Figure S21a](#)). Under this condition, 19% of BTO reaches T_c after 20 ps, while for $F_{\text{in}} = 1.4 \text{ mJcm}^{-2}$ the sample remains always below T_c ([Figure S22a](#)). Hence, a higher pump fluence leads to a larger portion of the BTO reaching higher temperatures and in shorter time. We note that when the pump photon energy E is below or $\lesssim 0.5 \text{ eV}$ above the bandgap E_g , peak power intensities in the range from kW cm^{-2} to GW cm^{-2} lead to a sample temperature increase below 50 K ^{12,14–16,19}. In our experiment, given the relatively high peak power intensity in the range $20\text{--}38 \text{ GW cm}^{-2}$, and the pump photon energy $\approx 1.2 \text{ eV}$ above the bandgap, sample heating is taken into account.

[Figure S21b](#) reports the strain map $\eta(z,t)$ in the BTO film based on the results of $T_p(z,t)$ and $T_e(z,t)$, with calculation details reported in [Supplementary Note 8](#). Here, it can be clearly seen how the regions of the sample below [above] T_c display smaller [larger] $\eta(z,t)$. In particular, for $t < 3.1 \text{ ps}$ the average strain $\bar{\eta}(t)$ is negative, primarily due to the compressive strain from the deformation potential ([Figure 1d](#)). Moreover, the three straight profiles in the [Figure S21b](#) mark the front of the strain wave propagating in the BTO at the sound speed and then reflected at the interface with SRO and air.

A few selected strain profiles at fixed delays are highlighted in [Figure S21c](#). Within the first 15 ps after $t = 0 \text{ ps}$ ([Supplementary Note 4](#)) the strain profile $\eta(z,t)$ undergoes relatively large changes resulting from the varying T_e and T_p , and the corresponding DP and TE contributions ([Figure S23](#)). After $\approx 15 \text{ ps}$ the strain profile reaches a metastable state at least for the following few tens of picoseconds. The maximum average tensile strain of this metastable state is directly proportional to the incident pump fluence and it depends on the film thickness ([Figure S21b-c](#) and [Figure S22b-c](#)).

From $\eta(z,t)$, we calculated $c(z,t) = c_0[\eta(z,t) + 1]$ for each unit cell along z and subsequently the diffraction profiles in the range $0 \text{ ps} < t < 20 \text{ ps}$ ([Figure S21d](#)). A selection of diffraction curves at different t ([Figure S21e](#)) are then compared to the experimental data ([Figure S21f](#)). The main features of the experimental data, i.e., the shift of the diffraction peak to smaller photon energies, the relative increase/decrease of the diffraction intensity on the low/high photon energy side, the larger broadening and smaller peak diffraction intensity as t increases, are all well reproduced by our simulations. This strongly corroborates the validity of the model employed to describe our data. The initial shift to higher photon energy for $t < 4 \text{ ps}$ is clearly shown by the increase of spectral weight around 1530 eV in [Figure S21d](#). Conversely, for $t > 4 \text{ ps}$, the average positive strain explains the peak shift to lower photon energy, and the strain gradient is the reason for the change in spectral weight from the high to the low energy side. At the same time, a larger strain gradient leads to broader diffraction curves, and given the conservation of the total area under the curve, to a smaller peak intensity. Qualitatively, the simulated diffraction curves show sharper oscillations, related to the small film thickness, as compared to the experimental ones ([Figure S21e-f](#)). This is the consequence of a slightly larger broadening of the experimental I_{XRD} curves that we assign to an initial strain profile $\eta(z,t = 0 \text{ ps}) \neq 0$, while we assume $\eta(z,t = 0 \text{ ps}) = 0$ throughout the sample for the simulated I_{XRD} curves ([Figure S24](#)). Finally, the discussion above regarding the incident pump fluence $F_{\text{in}} = 2.7 \text{ mJcm}^{-2}$ applies also to the lower fluence $F_{\text{in}} = 1.4 \text{ mJcm}^{-2}$. Also in the latter case, we find an excellent agreement between experiments and simulations

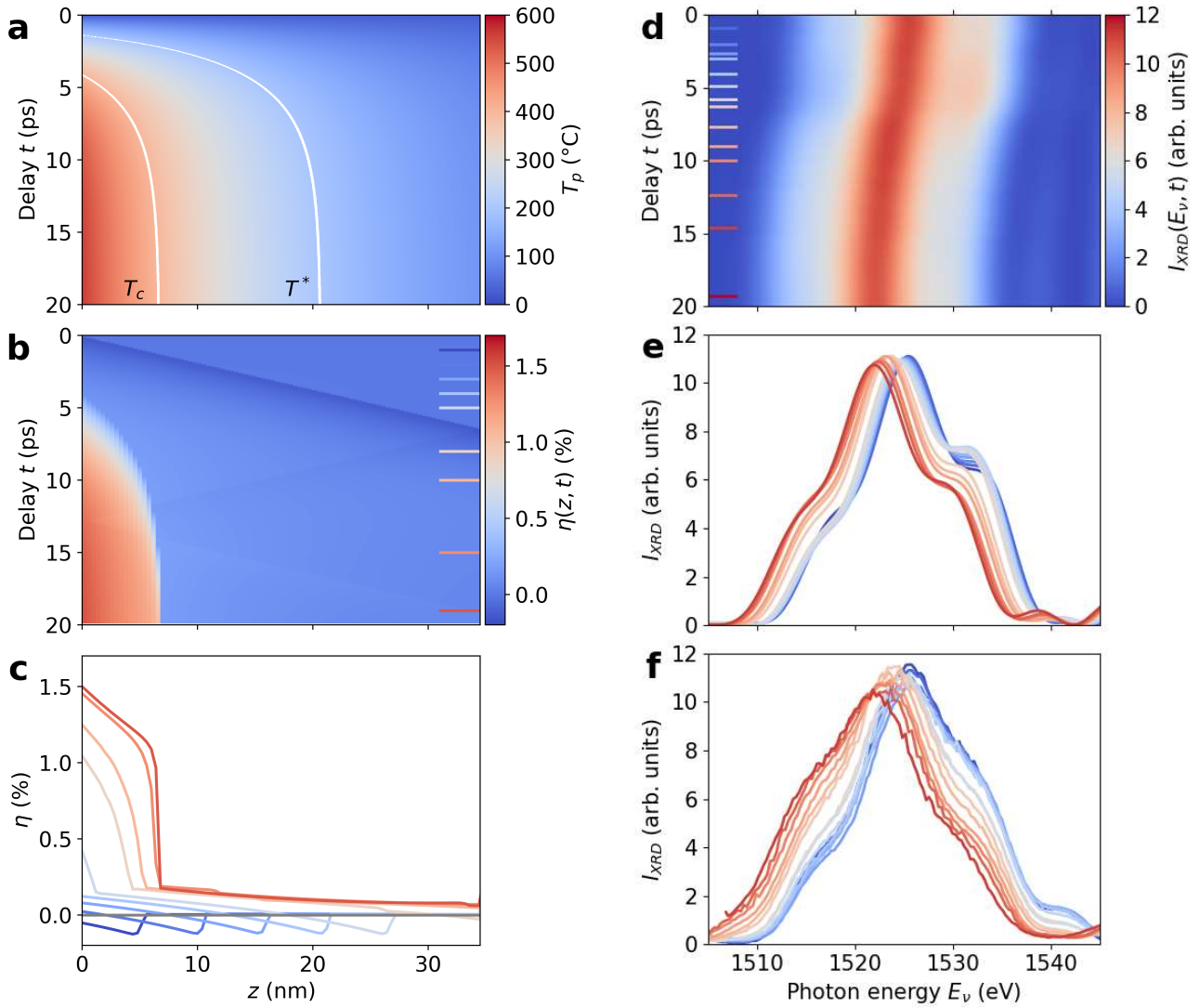


Figure S21. Temporal and spatial dependence of lattice temperature and strain, and diffraction curves at fixed delays, with $F_{\text{in}} = 2.7 \text{ mJ cm}^{-2}$. (a) 2D map of the lattice temperature T_p as a function of the delay t and the distance z from the BTO surface. The white lines indicate the Curie temperature $T_c = 400^\circ\text{C}$ and $T^* = 200^\circ\text{C}$ (Figure S4). (b) 2D map of the BTO strain $\eta(z, t)$ as a function of t and z . (c) Strain profiles $\eta(z, t)$ at time delays t marked in the panel (b). (d) 2D map of the simulated diffraction curves $I_{\text{XRD}}(t)$ as a function of delay t and photon energy E_V . (e) Simulated diffraction curves $I_{\text{XRD}}(E_V)$ at time delays t marked in panel (d). (f) Experimental diffraction curves at time delays t marked in panel (d). The data shown here refer to the incident pump fluence $F_{\text{in}} = 2.7 \text{ mJ cm}^{-2}$ and results from the solution of the 2TM and the 1D strain wave equation (Supplementary Note 7 and Supplementary Note 8).

(Figure S22e-f).

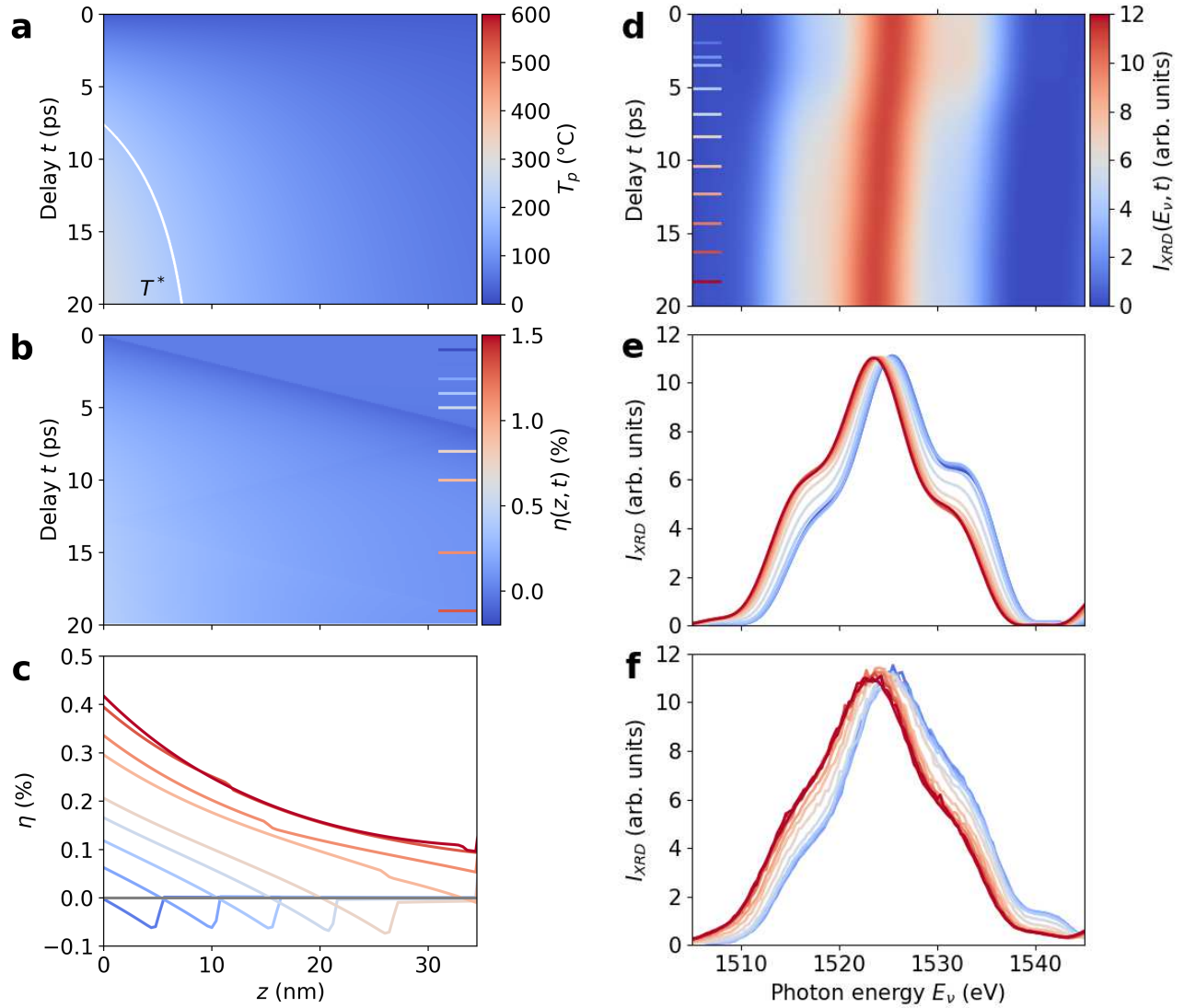


Figure S22. Temporal and spatial dependence of lattice temperature and strain, and diffraction curves at fixed delays, with $F_{\text{in}} = 1.4 \text{ mJ cm}^{-2}$. (a) 2D map of the lattice temperature T_p as a function of the delay t and the distance z from the BTO surface. The white line indicates the temperature $T^* = 200^\circ\text{C}$ (Figure S4). (b) 2D map of the BTO strain $\eta(z, t)$ as a function of delay t and z . (c) Strain profiles $\eta(z, t)$ at time delays t marked in the panel (b). (d) 2D map of the simulated diffraction curves $I_{\text{XRD}}(t)$ as a function of delay t and photon energy E_ν . (e) Selected diffraction curves $I_{\text{XRD}}(E_\nu)$ at time delays t marked in panel (d). (f) Experimental diffraction curves at time delays t marked in panel (d). The data shown here refer to the incident pump fluence $F_{\text{in}} = 1.4 \text{ mJ cm}^{-2}$ and result from the solution of the 2TM and the 1D strain wave equation (Supplementary Note 7 and Supplementary Note 8).

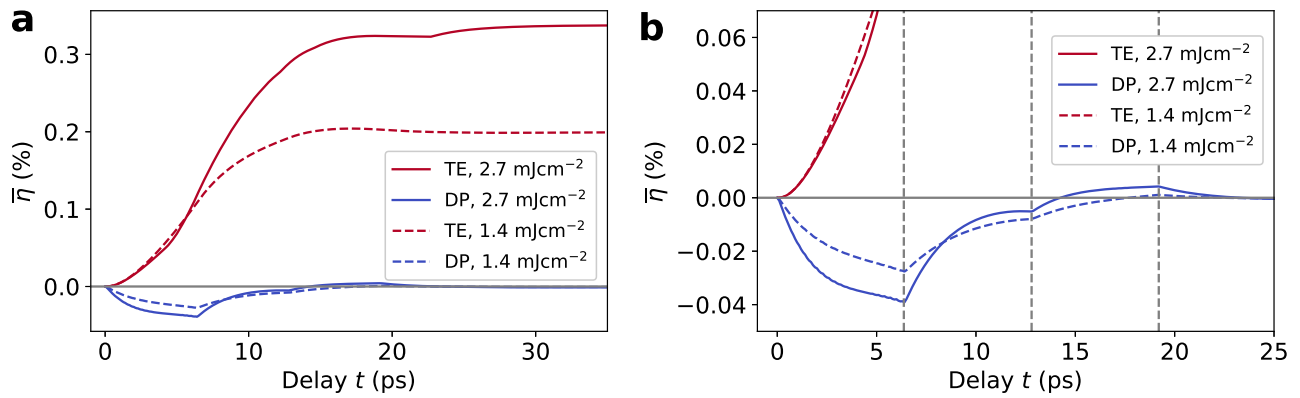


Figure S23. Deformation potential and thermoelastic contributions. (a): Thermoelastic (TE, red lines) and deformation potential (DP, blue lines) strain contributions at $F_{in} = 2.7 \text{ mJcm}^{-2}$ (solid lines) and $F_{in} = 1.4 \text{ mJcm}^{-2}$ (dashed lines). (b): same plot as in panel (a) with focus on the strain range $-0.05\% < \bar{\eta}(t) < 0.07\%$ and delay range $-1 \text{ ps} < t < 25 \text{ ps}$. The vertical gray dashed lines at 6.4 ps, 12.8 ps, 19.2 ps mark discontinuities in the DP strain profile, which are due to reflections of the DP strain wave at the BTO/SRO, BTO/air, and again BTO/SRO interfaces (Supplementary Note 6.1). The time constants result from the speed of sound in BTO (Table S2) multiplied by the traveled distance, which is d_{BTO} , $2d_{\text{BTO}}$ and $3d_{\text{BTO}}$, respectively. Discontinuities in the TE profile are too small to be seen because of the relatively large absolute value of the average TE strain that is mostly contributed by the BTO region near the surface (Figure S21b).

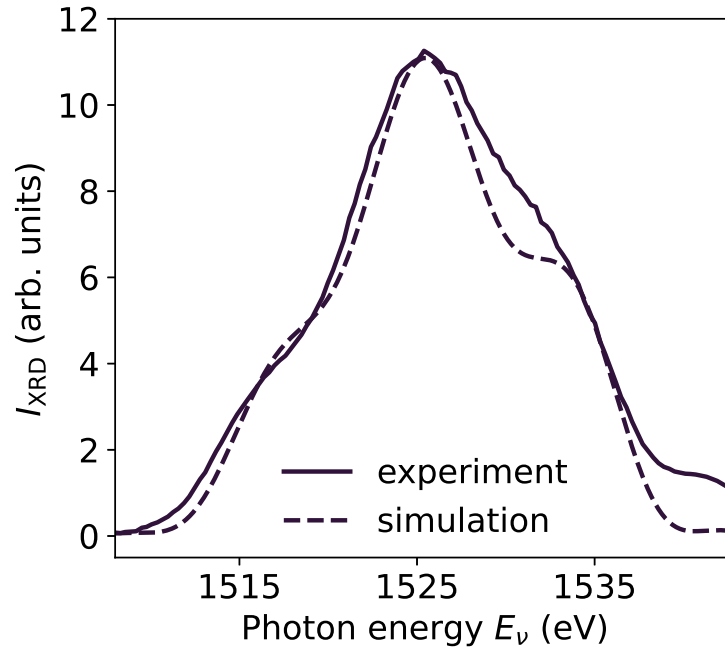


Figure S24. Comparison of simulated and experimental $I_{\text{XRD}}(E_v)$ at negative delay. Comparison of simulated (dashed line) and experimental (solid line) diffraction curve before the arrival of the pump laser. The broadening of the diffraction curves is calculated as $c_{\text{std}} = (1240000 \text{ eV pm}) / (2E_{v,\text{std}} \sin \theta)$, where $E_{v,\text{std}}$ is the standard deviation of energy values, around the (001) BTO peak, weighted by $I_{\text{XRD}}(E_v)$. Here, $c_{\text{std}} = 1.63 \text{ pm}$ and 1.80 pm for simulated and experimental curves, respectively. This is the consequence of a slightly larger broadening of the experimental I_{XRD} curve due to the presence of an initial strain profile $\bar{\eta} \neq 0$, while $\bar{\eta} = 0$ for the simulated I_{XRD} curve.

Supplementary Note 10 Estimation of the bandgap decrease

To estimate the largest bandgap decrease, first we determine the photoinduced electronic pressure as $\Delta P = \gamma_e C_e \Delta T_e \approx 1.7 \times 10^9 \text{ Pa}^4$, where $\gamma_e \approx 2.6^{87}$ is the Grüneisen parameter, C_e is the electronic heat capacity (Table S2), and $\Delta T_e = 1.56 \times 10^4 \text{ K}$ is the largest increase in electronic temperature of the BTO film averaged over d_{BTO} (Figure S17). Second, we express the bandgap variation as $\Delta E_g = \frac{\partial E_g}{\partial P} \Delta P \approx -3.2 \text{ meV}$, where $\frac{\partial E_g}{\partial P} = -3.0(5) \times 10^{-31} \text{ J Pa}^{-1}$ (Table S3).

Supplementary Note 11 Estimation of the electronic contribution to the ferroelectric polarization P_s

To quantify the relative contribution of structural ($\Delta P_s^\eta / P_s$) and electronic ($\Delta P_s^{ne} / P_{s,0}$) changes to the total polarization variation out of equilibrium $\Delta P_s / P_{s,0} = (\Delta P_s^\eta + \Delta P_s^{ne}) / P_{s,0} = \Delta P_s^\eta / P_{s,0} (1 + C_{ne})$, we first estimate $\Delta P_s^\eta / P_{s,0}$, and then derive the relative magnitude of the electronic contribution $C_{ne} = (\Delta P_s^{ne} / P_{s,0}) / (\Delta P_s^\eta / P_{s,0})$. From polarization-electric field hysteresis loops on differently strained BTO thin films grown on a GSO substrate²⁶, the relative change of the polarization as a function of the strain was determined to be $\Delta P_s^\eta / \Delta \eta = 15 \mu\text{C}/\text{cm}^2/\%$. In our data, at short time delays ($t < 4 \text{ ps}$) the strain experiences a marginal change $\Delta \bar{\eta} < 0.02\%$ and ΔP_s is clearly dominated by the presence of photoexcited carriers in the conduction band (Figure 2e-f). At larger time delays ($t \approx 20 \text{ ps}$), $\bar{\eta}$ reaches the saturation value of 0.34%, which would correspond to an increase in polarization of $\Delta P_s^\eta = 5.1 \mu\text{C cm}^{-2}$ ($\Delta P_s^\eta / P_{s,0} \approx 25\%$), assuming a polarization at equilibrium of $P_{s,0} \approx 20 \mu\text{C cm}^{-2}$ as found for BTO/SRO/GSO²⁶. In contrast, we measure an overall polarization change of $\Delta P_s / P_{s,0} \approx -2.5\%$ (Figure 2e). As a result, it follows that the electronic contribution C_{ne} , responsible for the reduced polarization, has $\approx 10\%$ larger magnitude than the structural one even at 20 ps ($C_{ne} \approx -1.1$).

References

1. Martin, L. W. & Rappe, A. M. Thin-film ferroelectric materials and their applications. *Nat. Rev. Mater.* **2**, 16087, DOI: [10.1038/natrevmats.2016.87](https://doi.org/10.1038/natrevmats.2016.87) (2017).
2. Kim, I. & Lee, J. Ferroelectric Transistors for Memory and Neuromorphic Device Applications. *Adv. Mater.* **35**, 2206864, DOI: [10.1002/adma.202206864](https://doi.org/10.1002/adma.202206864) (2023).
3. Guo, J. *et al.* Recent Progress in Optical Control of Ferroelectric Polarization. *Adv. Opt. Mater.* **9**, 2002146, DOI: [10.1002/adom.202002146](https://doi.org/10.1002/adom.202002146) (2021).
4. Ruello, P. & Gusev, V. E. Physical mechanisms of coherent acoustic phonons generation by ultrafast laser action. *Ultrasonics* **56**, 21–35, DOI: [10.1016/j.ultras.2014.06.004](https://doi.org/10.1016/j.ultras.2014.06.004) (2015).
5. Korff Schmising, C. v. *et al.* Coupled Ultrafast Lattice and Polarization Dynamics in Ferroelectric Nanolayers. *Phys. Rev. Lett.* **98**, 257601, DOI: [10.1103/PhysRevLett.98.257601](https://doi.org/10.1103/PhysRevLett.98.257601) (2007).
6. Schick, D. *et al.* Ultrafast lattice response of photoexcited thin films studied by X-ray diffraction. *Struct. dyn.* **1**, 064501, DOI: [10.1063/1.4901228](https://doi.org/10.1063/1.4901228) (2014).
7. Sheu, Y. M. *et al.* Using ultrashort optical pulses to couple ferroelectric and ferromagnetic order in an oxide heterostructure. *Nat. Commun.* **5**, 1–6, DOI: [10.1038/ncomms6832](https://doi.org/10.1038/ncomms6832) (2014).
8. Lee, H. J. *et al.* Structural Evidence for Ultrafast Polarization Rotation in Ferroelectric/Dielectric Superlattice Nanodomains. *Phys. Rev. X* **11**, 031031, DOI: [10.1103/PhysRevX.11.031031](https://doi.org/10.1103/PhysRevX.11.031031) (2021).
9. Li, T. *et al.* Optical control of polarization in ferroelectric heterostructures. *Nat. Commun.* **9**, 3344, DOI: [10.1038/s41467-018-05640-4](https://doi.org/10.1038/s41467-018-05640-4) (2018).
10. Ron, A. *et al.* Transforming a strain-stabilized ferroelectric into an intrinsic polar metal with light. *Phys. Rev. B* **108**, 224308, DOI: [10.1103/PhysRevB.108.224308](https://doi.org/10.1103/PhysRevB.108.224308) (2023).
11. Sarott, M. F. *et al.* Reversible Optical Control of Polarization in Epitaxial Ferroelectric Thin Films. *Adv. Mater.* **36**, 2312437, DOI: [10.1002/adma.202312437](https://doi.org/10.1002/adma.202312437) (2024).
12. Daranciang, D. *et al.* Ultrafast Photovoltaic Response in Ferroelectric Nanolayers. *Phys. Rev. Lett.* **108**, 087601, DOI: [10.1103/PhysRevLett.108.087601](https://doi.org/10.1103/PhysRevLett.108.087601) (2012).
13. Wen, H. *et al.* Electronic Origin of Ultrafast Photoinduced Strain in BiFeO₃. *Phys. Rev. Lett.* **110**, 037601, DOI: [10.1103/PhysRevLett.110.037601](https://doi.org/10.1103/PhysRevLett.110.037601) (2013).
14. Schick, D. *et al.* Localized Excited Charge Carriers Generate Ultrafast Inhomogeneous Strain in the Multiferroic BiFeO₃. *Phys. Rev. Lett.* **112**, 097602, DOI: [10.1103/PhysRevLett.112.097602](https://doi.org/10.1103/PhysRevLett.112.097602) (2014).
15. Matzen, S. *et al.* Tuning Ultrafast Photoinduced Strain in Ferroelectric-Based Devices. *Adv. Electron. Mater.* **5**, 1800709, DOI: [10.1002/aelm.201800709](https://doi.org/10.1002/aelm.201800709) (2019).

16. Ahn, Y. *et al.* Dynamic Tilting of Ferroelectric Domain Walls Caused by Optically Induced Electronic Screening. *Phys. Rev. Lett.* **127**, 097402, DOI: [10.1103/PhysRevLett.127.097402](https://doi.org/10.1103/PhysRevLett.127.097402) (2021).
17. Sri Gyan, D. *et al.* Optically Induced Picosecond Lattice Compression in the Dielectric Component of a Strongly Coupled Ferroelectric/Dielectric Superlattice. *Adv. Electron. Mater.* **8**, 2101051, DOI: [10.1002/aelm.202101051](https://doi.org/10.1002/aelm.202101051) (2022).
18. Gu, R. *et al.* Temporal and spatial tracking of ultrafast light-induced strain and polarization modulation in a ferroelectric thin film. *Sci. Adv.* **9**, DOI: [10.1126/sciadv.adi1160](https://doi.org/10.1126/sciadv.adi1160) (2023).
19. Ganguly, S. *et al.* Photostrictive Actuators Based on Freestanding Ferroelectric Membranes. *Adv. Mater.* **36**, 2310198, DOI: [10.1002/adma.202310198](https://doi.org/10.1002/adma.202310198) (2024).
20. Chen, F. *et al.* Ultrafast terahertz-field-driven ionic response in ferroelectric BaTiO₃. *Phys. Rev. B* **94**, 180104, DOI: [10.1103/PhysRevB.94.180104](https://doi.org/10.1103/PhysRevB.94.180104) (2016).
21. Mankowsky, R., von Hoegen, A., Först, M. & Cavalleri, A. Ultrafast Reversal of the Ferroelectric Polarization. *Phys. Rev. Lett.* **118**, 197601, DOI: [10.1103/PhysRevLett.118.197601](https://doi.org/10.1103/PhysRevLett.118.197601) (2017).
22. Yang, Y., Paillard, C., Xu, B. & Bellaiche, L. Photostriction and elasto-optic response in multiferroics and ferroelectrics from first principles. *J. Phys.: Condens. Matter* **30**, 073001, DOI: [10.1088/1361-648X/aaa51f](https://doi.org/10.1088/1361-648X/aaa51f) (2018).
23. Devonshire, A. XCVI. Theory of barium titanate: Part I. *The London, Edinburgh, Dublin Philos. Mag. J. Sci.* **40**, 1040–1063, DOI: [10.1080/14786444908561372](https://doi.org/10.1080/14786444908561372) (1949).
24. Choi, K. J. *et al.* Enhancement of Ferroelectricity in Strained BaTiO₃ Thin Films. *Science* **306**, 1005–1009, DOI: [10.1126/science.1103218](https://doi.org/10.1126/science.1103218) (2004).
25. Dawber, M. *et al.* Tailoring the Properties of Artificially Layered Ferroelectric Superlattices. *Adv. Mater.* **19**, 4153–4159, DOI: [10.1002/adma.200700965](https://doi.org/10.1002/adma.200700965) (2007).
26. Pesquera, D. *et al.* Beyond Substrates: Strain Engineering of Ferroelectric Membranes. *Adv. Mater.* **32**, 2003780, DOI: [10.1002/adma.202003780](https://doi.org/10.1002/adma.202003780) (2020).
27. Zhang, Y. *et al.* Probing Ultrafast Dynamics of Ferroelectrics by Time-Resolved Pump-Probe Spectroscopy. *Adv. Sci.* **8**, 2102488, DOI: [10.1002/advs.202102488](https://doi.org/10.1002/advs.202102488) (2021).
28. Chernova, E. *et al.* Strain-controlled optical absorption in epitaxial ferroelectric BaTiO₃ films. *Appl. Phys. Lett.* **106**, 192903, DOI: [10.1063/1.4921083](https://doi.org/10.1063/1.4921083) (2015).
29. Lian, C., Ali, Z. A., Kwon, H. & Wong, B. M. Indirect but Efficient: Laser-Excited Electrons Can Drive Ultrafast Polarization Switching in Ferroelectric Materials. *J. Phys. Chem. Lett.* **10**, 3402–3407, DOI: [10.1021/acs.jpcclett.9b01046](https://doi.org/10.1021/acs.jpcclett.9b01046) (2019).
30. Chen, J., Hong, L., Huang, B. & Xiang, H. Ferroelectric switching assisted by laser illumination. *Phys. Rev. B* **109**, 094102, DOI: [10.1103/PhysRevB.109.094102](https://doi.org/10.1103/PhysRevB.109.094102) (2024).

31. Koleżyński, A. & Tkacz-Śmiech, K. From the Molecular Picture to the Band Structure of Cubic and Tetragonal Barium Titanate. *Ferroelectrics* **314**, 123–134, DOI: [10.1080/00150190590926300](https://doi.org/10.1080/00150190590926300) (2005).
32. Wright, O. B. & Gusev, V. E. Acoustic generation in crystalline silicon with femtosecond optical pulses. *Appl. Phys. Lett.* **66**, 1190–1192, DOI: [10.1063/1.113853](https://doi.org/10.1063/1.113853) (1995).
33. Khenata, R. *et al.* First-principle calculations of structural, electronic and optical properties of BaTiO₃ and BaZrO₃ under hydrostatic pressure. *Solid State Commun.* **136**, 120–125, DOI: [10.1016/j.ssc.2005.04.004](https://doi.org/10.1016/j.ssc.2005.04.004) (2005).
34. Chen, L. Y. *et al.* Ultrafast photoinduced mechanical strain in epitaxial BiFeO₃ thin films. *Appl. Phys. Lett.* **101**, 041902, DOI: [10.1063/1.4734512](https://doi.org/10.1063/1.4734512) (2012).
35. Jin, Z. *et al.* Structural dependent ultrafast electron-phonon coupling in multiferroic BiFeO₃ films. *Appl. Phys. Lett.* **100**, 071105, DOI: [10.1063/1.3685496](https://doi.org/10.1063/1.3685496) (2012).
36. Sheu, Y. M. *et al.* Ultrafast carrier dynamics and radiative recombination in multiferroic BiFeO₃. *Appl. Phys. Lett.* **100**, 242904, DOI: [10.1063/1.4729423](https://doi.org/10.1063/1.4729423) (2012).
37. Wang, K. *et al.* Coupling Among Carriers and Phonons in Femtosecond Laser Pulses Excited SrRuO₃: A Promising Candidate for Optomechanical and Optoelectronic Applications. *ACS Appl. Nano Mater.* **2**, 3882–3888, DOI: [10.1021/acsanm.9b00728](https://doi.org/10.1021/acsanm.9b00728) (2019).
38. Mudiyansele, R. R. H. H. *et al.* Coherent acoustic phonons and ultrafast carrier dynamics in heteroepitaxial BaTiO₃–BiFeO₃ films and nanorods. *J. Mater. Chem. C* **7**, 14212–14222, DOI: [10.1039/C9TC01584A](https://doi.org/10.1039/C9TC01584A) (2019).
39. Denev, S. A., Lummen, T. T. A., Barnes, E., Kumar, A. & Gopalan, V. Probing Ferroelectrics Using Optical Second Harmonic Generation. *J. Am. Ceram. Soc.* **94**, 2699–2727, DOI: [10.1111/j.1551-2916.2011.04740.x](https://doi.org/10.1111/j.1551-2916.2011.04740.x) (2011).
40. Murgan, R., Tilley, D. R., Ishibashi, Y., Webb, J. F. & Osman, J. Calculation of nonlinear-susceptibility tensor components in ferroelectrics: cubic, tetragonal, and rhombohedral symmetries. *J. Opt. Soc. Am. B* **19**, 2007, DOI: [10.1364/JOSAB.19.002007](https://doi.org/10.1364/JOSAB.19.002007) (2002).
41. Thomsen, C., Grahn, H. T., Maris, H. J. & Tauc, J. Surface generation and detection of phonons by picosecond light pulses. *Phys. Rev. B* **34**, 4129–4138, DOI: [10.1103/PhysRevB.34.4129](https://doi.org/10.1103/PhysRevB.34.4129) (1986).
42. Young, E. S. K., Akimov, A. V., Champion, R. P., Kent, A. J. & Gusev, V. Picosecond strain pulses generated by a supersonically expanding electron-hole plasma in GaAs. *Phys. Rev. B* **86**, 155207, DOI: [10.1103/PhysRevB.86.155207](https://doi.org/10.1103/PhysRevB.86.155207) (2012).
43. Gattinoni, C. *et al.* Interface and surface stabilization of the polarization in ferroelectric thin films. *PNAS* **117**, 28589–28595, DOI: [10.1073/pnas.2007736117](https://doi.org/10.1073/pnas.2007736117) (2020).
44. Wang, Y., Liu, X., Burton, J. D., Jaswal, S. S. & Tsymbal, E. Y. Ferroelectric Instability Under Screened Coulomb Interactions. *Phys. Rev. Lett.* **109**, 247601, DOI: [10.1103/PhysRevLett.109.247601](https://doi.org/10.1103/PhysRevLett.109.247601) (2012).

45. Paillard, C., Torun, E., Wirtz, L., Íñiguez, J. & Bellaiche, L. Photoinduced Phase Transitions in Ferroelectrics. *Phys. Rev. Lett.* **123**, 087601, DOI: [10.1103/PhysRevLett.123.087601](https://doi.org/10.1103/PhysRevLett.123.087601) (2019).
46. Fridkin, V. M. Bulk photovoltaic effect in noncentrosymmetric crystals. *Crystallogr. Rep.* **46**, 654–658, DOI: [10.1134/1.1387133](https://doi.org/10.1134/1.1387133) (2001).
47. Dai, Z. & Rappe, A. M. Recent progress in the theory of bulk photovoltaic effect. *Chem. Phys. Rev.* **4**, 011303, DOI: [10.1063/5.0101513](https://doi.org/10.1063/5.0101513) (2023).
48. Matsuo, H. & Noguchi, Y. Bulk photovoltaic effect in ferroelectrics. *Jpn. J. Appl. Phys.* **63**, 060101, DOI: [10.35848/1347-4065/ad442e](https://doi.org/10.35848/1347-4065/ad442e) (2024).
49. Koch, W. T. H., Munser, R., Ruppel, W. & Würfel, P. Bulk photovoltaic effect in BaTiO₃. *Solid State Commun.* **17**, 847–850, DOI: [10.1016/0038-1098\(75\)90735-8](https://doi.org/10.1016/0038-1098(75)90735-8) (1975).
50. Koch, W. T. H., Munser, R., Ruppel, W. & Würfel, P. Anomalous photovoltage in BaTiO₃. *Ferroelectrics* **13**, 305–307, DOI: [10.1080/00150197608236596](https://doi.org/10.1080/00150197608236596) (1976).
51. Kundys, B., Viret, M., Colson, D. & Kundys, D. O. Light-induced size changes in BiFeO₃ crystals. *Nat. Mater.* **9**, 803–805, DOI: [10.1038/nmat2807](https://doi.org/10.1038/nmat2807) (2010).
52. Young, S. M. & Rappe, A. M. First Principles Calculation of the Shift Current Photovoltaic Effect in Ferroelectrics. *Phys. Rev. Lett.* **109**, 116601, DOI: [10.1103/PhysRevLett.109.116601](https://doi.org/10.1103/PhysRevLett.109.116601) (2012).
53. Sanna, S., Thierfelder, C., Wippermann, S., Sinha, T. P. & Schmidt, W. G. Barium titanate ground- and excited-state properties from first-principles calculations. *Phys. Rev. B* **83**, 054112, DOI: [10.1103/PhysRevB.83.054112](https://doi.org/10.1103/PhysRevB.83.054112) (2011).
54. Paillard, C., Xu, B., Dkhil, B., Geneste, G. & Bellaiche, L. Photostriction in Ferroelectrics from Density Functional Theory. *Phys. Rev. Lett.* **116**, 247401, DOI: [10.1103/PhysRevLett.116.247401](https://doi.org/10.1103/PhysRevLett.116.247401) (2016).
55. Wen, Y.-C. *et al.* Efficient generation of coherent acoustic phonons in (111) InGaAs/GaAs multiple quantum wells through piezoelectric effects. *Appl. Phys. Lett.* **90**, 172102, DOI: [10.1063/1.2731441](https://doi.org/10.1063/1.2731441) (2007).
56. Li, T., Deng, S., Liu, H. & Chen, J. Insights into Strain Engineering: From Ferroelectrics to Related Functional Materials and Beyond. *Chem. Rev.* **124**, 7045–7105, DOI: [10.1021/acs.chemrev.3c00767](https://doi.org/10.1021/acs.chemrev.3c00767) (2024).
57. Zhao, T., Lu, H., Chen, F., Yang, G. & Chen, Z. Stress-induced enhancement of second-order nonlinear optical susceptibilities of barium titanate films. *J. Appl. Phys.* **87**, 7448–7451, DOI: [10.1063/1.373008](https://doi.org/10.1063/1.373008) (2000).
58. Jeong, J.-W., Shin, S.-C., Lyubchanskii, I. L. & Varyukhin, V. N. Strain-induced three-photon effects. *Phys. Rev. B* **62**, 13455–13463, DOI: [10.1103/PhysRevB.62.13455](https://doi.org/10.1103/PhysRevB.62.13455) (2000).
59. Birkholz, M. *Thin Film Analysis by X-Ray Scattering* (Wiley-VCH, Weinheim, 2005).
60. Young, R. A. & Wiles, D. B. Profile shape functions in Rietveld refinements. *J. Appl. Crystallogr.* **15**, 430–438, DOI: <https://doi.org/10.1107/S002188988201231X> (1982).

61. Rodriguez, B. J., Callahan, C., Kalinin, S. V. & Proksch, R. Dual-frequency resonance-tracking atomic force microscopy. *Nanotechnology* **18**, 475504, DOI: <https://doi.org/10.1088/0957-4484/18/47/475504> (2007).
62. Löhl, F. *et al.* Electron Bunch Timing with Femtosecond Precision in a Superconducting Free-Electron Laser. *Phys. Rev. Lett.* **104**, 144801, DOI: [10.1103/PhysRevLett.104.144801](https://doi.org/10.1103/PhysRevLett.104.144801) (2010).
63. Czwalińska, M. *et al.* Beam Arrival Stability at the European XFEL. *Proc. 12th Int. Part. Accel. Conf. IPAC2021* (2021).
64. Carley, R., Van Kuiken, B., Le Guyader, L., Mercurio, G. & Scherz, A. (eds.) *SCS Instrument Review Report* (European X-Ray Free-Electron Laser Facility GmbH, Schenefeld, 2022).
65. Schneidmiller, E. A. & Yurkov, M. V. Photon beam properties at the European XFEL (December 2010 revision). *TESLA-FEL 2010-06* 127 (2010).
66. Gerasimova, N. *et al.* The soft X-ray monochromator at the SASE3 beamline of the European XFEL: from design to operation. *J. Synchrotron Radiat.* **29**, 1299–1308, DOI: [10.1107/S1600577522007627](https://doi.org/10.1107/S1600577522007627) (2022).
67. Zhang, Y. *et al.* Characterization of domain distributions by second harmonic generation in ferroelectrics. *Npj Comput. Mater.* **4**, 39, DOI: [10.1038/s41524-018-0095-6](https://doi.org/10.1038/s41524-018-0095-6) (2018).
68. Thompson, J. *et al.* Enhanced metallic properties of SrRuO₃ thin films via kinetically controlled pulsed laser epitaxy. *Appl. Phys. Lett.* **109**, 161902, DOI: [10.1063/1.4964882](https://doi.org/10.1063/1.4964882) (2016).
69. Yamanaka, S. *et al.* Thermophysical properties of SrHfO₃ and SrRuO₃. *J. Solid State Chem.* **177**, 3484–3489, DOI: [10.1016/j.jssc.2004.05.039](https://doi.org/10.1016/j.jssc.2004.05.039) (2004).
70. Hidde, J., Gugushev, C., Ganschow, S. & Klimm, D. Thermal conductivity of rare-earth scandates in comparison to other oxidic substrate crystals. *J. Alloy. Compd.* **738**, 415–421, DOI: [10.1016/j.jallcom.2017.12.172](https://doi.org/10.1016/j.jallcom.2017.12.172) (2018).
71. de Jong, M. *et al.* Charting the complete elastic properties of inorganic crystalline compounds. *Sci. Data* **2**, 150009, DOI: [10.1038/sdata.2015.9](https://doi.org/10.1038/sdata.2015.9) (2015).
72. Mills, I., International Union of Pure and Applied Chemistry & International Union of Pure and Applied Chemistry (eds.) *Quantities, units, and symbols in physical chemistry* (1993), 2nd ed edn.
73. He, Y. Heat capacity, thermal conductivity, and thermal expansion of barium titanate-based ceramics. *Thermochim. Acta* **419**, 135–141, DOI: [10.1016/j.tca.2004.02.008](https://doi.org/10.1016/j.tca.2004.02.008) (2004).
74. Anisimov, S. I., Kapeliovich, B. L. & Perelman, T. L. Electron emission from metal surfaces exposed to ultrashort laser pulses. *Zh. Eksp. Teor. Fiz* **66**, 375–7 (1974).
75. Müller, A. & Härdtl, K. H. Ambipolar diffusion phenomena in BaTiO₃ and SrTiO₃. *Appl. Phys. A* **49**, 75–82, DOI: [10.1007/BF00615468](https://doi.org/10.1007/BF00615468) (1989).
76. Wang, Z., Yang, M. & Zhang, H. Strain engineering on electrocaloric effect in PbTiO₃ and BaTiO₃. *Adv. Compos. Hybrid Mater.* **4**, 1239–1247, DOI: [10.1007/s42114-021-00257-6](https://doi.org/10.1007/s42114-021-00257-6) (2021).

77. de Ligny, D. & Richet, P. High-temperature heat capacity and thermal expansion of SrTiO₃ and SrZrO₃ perovskites. *Phys. Rev. B* **53**, 3013–3022, DOI: [10.1103/PhysRevB.53.3013](https://doi.org/10.1103/PhysRevB.53.3013) (1996).
78. Guyot, F., Richet, P., Courtial, P. & Gillet, P. High-temperature heat capacity and phase transitions of CaTiO₃ perovskite. *Phys. Chem. Miner.* **20** (1993).
79. Vladimirov, V. S. (ed.) *A Collection of Problems on the Equations of Mathematical Physics* (Springer Berlin Heidelberg, Berlin, Heidelberg, 1986).
80. Lin, Z., Zhigilei, L. V. & Celli, V. Electron-phonon coupling and electron heat capacity of metals under conditions of strong electron-phonon nonequilibrium. *Phys. Rev. B* **77**, 075133, DOI: [10.1103/PhysRevB.77.075133](https://doi.org/10.1103/PhysRevB.77.075133) (2008).
81. Wang, X. Y., Riffe, D. M., Lee, Y.-S. & Downer, M. C. Time-resolved electron-temperature measurement in a highly excited gold target using femtosecond thermionic emission. *Phys. Rev. B* **50**, 8016–8019, DOI: [10.1103/PhysRevB.50.8016](https://doi.org/10.1103/PhysRevB.50.8016) (1994).
82. Rumble, J. R. (ed.) *CRC Handbook of Chemistry and Physics* (CRC Press, 2023), 104th edn.
83. Fundamental Physical Constants from NIST.
84. Chan, C. C. S. *et al.* Uncovering the Electron-Phonon Interplay and Dynamical Energy-Dissipation Mechanisms of Hot Carriers in Hybrid Lead Halide Perovskites. *Adv. Energy Mater.* **11**, 2003071, DOI: [10.1002/aenm.202003071](https://doi.org/10.1002/aenm.202003071) (2021).
85. Elsayed-Ali, H. E., Norris, T. B., Pessot, M. A. & Mourou, G. A. Time-resolved observation of electron-phonon relaxation in copper. *Phys. Rev. Lett.* **58**, 1212–1215, DOI: [10.1103/PhysRevLett.58.1212](https://doi.org/10.1103/PhysRevLett.58.1212) (1987).
86. Hohlfeld, J. *et al.* Electron and lattice dynamics following optical excitation of metals. *Chem. Phys.* **251**, 237–258, DOI: [10.1016/S0301-0104\(99\)00330-4](https://doi.org/10.1016/S0301-0104(99)00330-4) (2000).
87. Choithrani, R. Structural, elastic and thermal properties of batio3. *Invertis J. Sci. & Technol.* **7**, 72–77 (2014).